Aerosol Science and Technology, 39:1143–1163, 2005

ISSN: 0278-6826 print / 1521-7388 online
DOI: 10.1080/02786820500423782

Design, Modeling, Optimization, and Experimental Tests of a Particle Beam Width Probe for the Aerodyne Aerosol Mass Spectrometer

J. Alex Huffman,[1] John T. Jayne,[2] Frank Drewnick,[3] Allison C. Aiken,[1] Timothy Onasch,[2] Douglas R. Worsnop,[2] and Jose L. Jimenez[1]

[1]*Department of Chemistry and Biochemistry, and Cooperative Institute for Research in the Environmental Sciences (CIRES), University of Colorado, Boulder, Colorado, USA*
[2]*Aerodyne Research Inc., Billerica, Massachusetts, USA*
[3]*Max Planck Institute for Chemistry, Mainz, Germany*

Aerodynamic lens inlets have revolutionized aerosol mass spectrometry by allowing the introduction of a very narrow particle beam into a vacuum chamber for subsequent analysis. The real-time measurement of particle beam width after an aerodynamic lens is of interest for two reasons: (1) it allows a correction to be made to the measured particle concentration if the beam is so broad, due to poor focusing by non-spherical particles, that some particles miss the detection system; and (2) under constant lens pressure it can provide a surrogate particle non-sphericity measurement. For these reasons, a beam width probe (BWP) has been designed and implemented for the Aerodyne Aerosol Mass Spectrometer (AMS), although this approach is also applicable to other instruments that use aerodynamic lens inlets. The probe implemented here consists of a thin vertical wire that can be precisely positioned to partially block the particle beam at fixed horizontal locations in order to map out the width of the particle beam. A computer model was developed to optimize the BWP and interpret its experimental data. Model assumptions were found to be reasonably accurate for all laboratory-generated particle types to which the model was compared. Comparisons of particle beam width data from a number of publications are also shown here. Particle losses due to beam broadening are found to be minor for the AMS for both laboratory and ambient particles. The model was then used to optimize the choice of the BWP dimensions, and to guide its use during continuous operation. A wire diameter approximately 1.55 times larger than the beam width to be measured provides near optimal sensitivity toward both collection efficiency and surrogate non-sphericity information. Wire diameters of 0.62 mm and 0.44 mm (for the AMS "long" and "short" chambers, respectively) provide reasonable sensitivity over the expected range of particle beam widths, for both spherical and non-spherical particles. Three other alternative BWP geometries were also modeled and discussed.

Received 10 April 2005; accepted 19 October 2005.

The authors thank Jay Slowik of Boston College for use of propane flame-generated soot data, Dara Salcedo of the Centro de Investigaciones Químicas, Universidad Autónoma del Estado de Morelos, Cuernavaca, Morelos, México for use of ambient Mexico City data, as well as Ann Middlebrook, Dan Murphy and Dan Cizczo of NOAA, Alice Delia of the University of Colorado, James Allan of the University of Manchester, the AMS Users Community, and the Jimenez Research Group for helpful discussions. We also thank NASA Earth System Science (grant NNG04GA67G) and EPA (grant EP-D-04-008) for funding. J. Alex Huffman and Allison Aiken are grateful for NASA Graduate Fellowships (grants NGT5-30516 and NNG04GR06H respectively).

Address correspondence to Jose-Luis Jimenez, Department Chemistry & Biochemistry, and Cooperative Institute for Research in the Environmental Sciences (CIRES), Boulder, CO, USA. E-mail: jose.jimenez@colorado.edu

1. INTRODUCTION

The development of aerodynamic lens inlets in the last decade has revolutionized the way particles can be focused into very narrow beams for subsequent analysis. Aerodynamic lenses were first demonstrated by the group of P.H. McMurry at the University of Minnesota (Liu et al. 1995a, 1995b) and have been the subject of a number of characterization and customization studies by several groups (Petrucci et al. 2000; Schreiner et al. 1999; Schreiner et al. 1998; Tafreshi et al. 2002; Zhang et al. 2002; Zhang et al. 2004c). A multistage lens consists of a cylindrical tube through which a series of axisymmetric cylindrical constrictions act to compress the gas (and particle) trajectories, while a final nozzle is used for the expansion of the gas and particle beam into the vacuum chamber. This results in focusing of particles within a given size range based on particle Stokes number. The particle-focusing characteristics of the lens are dependent on both the size and shape of the particles, as discussed in more detail below.

As particles exit the aerodynamic lens into a vacuum chamber, the beam is tightly focused ($\sim$100 μm diameter for Liu-type lenses, (Heberlein et al. 2001)), but small radial velocity components due to imperfect aerodynamic focusing and Brownian motion act to slightly broaden the beam as it travels under vacuum. "Lift" forces on irregular particles result in additional radial velocity components and divergence of the particle trajectories

TABLE 1
Particle flight distance, vaporizer (or laser spot) size, and solid angles of collection for the detection geometries of the long-chamber and short-chamber AMS, and two laser ablation particle mass spectrometers (Cziczo et al. 2003; Gard et al. 1997). The solid angle of detection represents the geometric area sampled by the vaporization laser or vaporizer at the given particle flight distance from the lens exit

Instrument used as model of detection geometry	Distance from lens to vaporizer or ablation laser (mm)	Distance from lens to BWP (mm)	Laser Spot/ vaporizer width (mm)	Solid angle of detection, ω (sr)
"Long" AMS	450	353	3.81	5.6×10^{-5}
"Short" AMS	348	251	3.81	9.3×10^{-5}
Design # 1	40	—	0.15	1.1×10^{-5}
Design # 2	200	—	0.4	3.1×10^{-6}

(Liu et al. 1995a). For this reason, beams comprised of spherical particles have the tightest focusing for a given particle size, and broader beams are observed when sampling irregular particles (Jayne et al. 2000; Kane and Johnston 2000; Liu et al. 1995b; Schreiner et al. 1998; Tobias et al. 2000). This beam broadening has two practical implications: (1) the beam solid angle may become so large that a measurable fraction of particles may miss the detection system in some instruments, resulting in a sampling bias correlated with particle shape (and also with composition if shape and composition are related); and (2) the degree of beam broadening with respect to spherical particles of the same size can be used as a real-time surrogate measurement of particle non-sphericity (under constant lens pressure conditions).

Currently, many particle mass spectrometers utilize aerodynamic lenses in order to introduce particles into a vacuum system for real-time analysis (Cziczo et al. 2003; Jayne et al. 2000; Mahadevan et al. 2002; Oktem et al. 2004; Schreiner et al. 2002; Su et al. 2004; Svane et al. 2004; Sykes et al. 2002; Tobias et al. 2000; Zelenyuk et al. 1999). The Aerodyne Aerosol Mass Spectrometer (AMS) has recently been commercialized and it is currently the most commonly used real-time particle mass spectrometer. The AMS can provide real-time information on mass concentrations of chemical species in/on submicron aerosols, as well as on chemically resolved size distributions (Jayne et al. 2000; Jimenez et al. 2003b). Submicron aerosols entering the AMS are focused into a narrow beam via an aerodynamic lens (Zhang et al. 2002, 2004c), and reach a terminal velocity that is a function of their vacuum aerodynamic diameter, d_{va} (DeCarlo et al. 2004; Jimenez et al. 2003a). The AMS measures particle size by quantifying the time it takes the particles to arrive at the detector (Jayne et al. 2000; Jimenez et al. 2003b) after a known gate (chopper) opening time. Non-refractory particles that are sufficiently focused impact the vaporizer surface and are flash-vaporized at a temperature of approximately 600°C. Approximately one out of every million of the vaporized molecules is ionized via electron-impact ionization (EI) at 70 eV. In the standard AMS ("Q-AMS") the ions formed are extracted into a quadrupole mass analyzer, and detected with an electron multiplier. A recently demonstrated ion time-of-flight AMS ("ToF-AMS") is identical in design to the Q-AMS except in that the quadrupole mass analyzer has been replaced by a time-of-flight mass analyzer (Drewnick et al. 2004). Sufficiently low pressures (10^{-7} to 10^{-8} Torr in the ionization region) are achieved via four layers of differential pumping (Jayne et al. 2000). Two different chamber lengths ("long" and "short") are currently in use. Table 1 shows the physical dimensions of the two AMS chamber designs, and Figure 1 shows a depiction of the chamber geometries and distances. Jayne et al. (2000) and Jimenez et al. (2003b) describe the instrument in more detail.

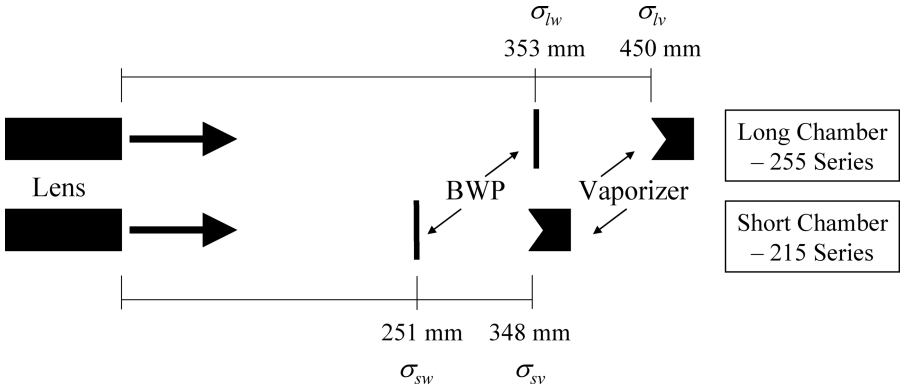

FIG. 1. Schematic diagram of relative location of vaporizer, and BWP for the two current AMS configurations. Beam widths, σ, are shown in the plane which they reference. See Table 3.

Fluid dynamic modeling results for the lens system implemented in the AMS, suggest 100% transmission for spherical particles for d_{va} of approximately 60–600 nm, with reduced transmission between approximately 30 (Zhang et al. 2004b) and 1500 nm, and allows the concentration of particles at the detector by a factor of approximately 10^7 over gas-phase molecules (Allan et al. 2004b; Jayne et al. 2000; Jimenez et al. 2003b). The particle flight length and vaporizer diameter in the long-chamber AMS were designed to provide 100% collection of several non-spherical particle types that had been identified early in the development of the instrument (Jayne et al. 2000). There is evidence from laboratory studies, however, that certain particle types (such as flame soot) can produce beams broad enough so that slightly less than 100% of the particles impact the vaporizer for the long-chamber AMS design (Slowik et al. 2004). A lack of detection for such non-spherical particles would result in a bias in their reported mass and number concentrations.

While the width of the beams produced by most particle types appears to be narrow enough for all particles to impact the AMS vaporizer, it is important to be able to verify this in real-time in the AMS and in other instruments that use aerodynamic lens inlets. Previous measurements of particle beam width were carried out by using a moveable knife-edge (Liu et al. 1995b; Schreiner et al. 1999; Schreiner et al. 1998) or wire (Jayne et al. 2000) to partially block the beam, while measuring the reduction in particle signal; by changing the lens aim, and measuring the resultant change in signal (Jayne et al. Aerodyne Research, unpublished results); qualitatively by measuring loss in total signal with respect to spherical particles (Tobias et al. 2000); and by measuring the hit rate by an ablation laser as it is translated across the particle beam (Kane and Johnston 2000; Su et al. 2004). Of those methods, the intermittent blockage of the particle beam is best suited to the rapid real-time measurement of particle beam width. Thus, in order to enable real-time quantification of surrogate particle non-sphericity and of the shape-related collection efficiency (E_s) of the AMS, a particle-beam width probe (BWP) has been designed and constructed. This paper presents a model of the effect of the particle BWP on particle signal as a function of particle beam and probe widths. The model is based on the assumption that particle density within the beam is described as a 2-D circular Gaussian distribution. This assumption is tested experimentally using monodisperse particles of several pure compositions. The model is then used to optimize the probe design, to study the collection of very irregular particle beams, and to evaluate alternative probe geometries. The results presented here focus on the AMS, but are applicable to many other instruments that use aerodynamic lens inlets.

2. METHODS

2.1 Definition of Particle Collection Efficiency due to Shape

To characterize the effect of shape on incomplete particle detection, we define here the AMS collection efficiency due to irregular shape, and as a function of particle size for a given particle composition and phase as $E_s(d_{va})$. This is the fraction of particles physically hitting the vaporizer, relative to spheres of the same vacuum aerodynamic diameter (d_{va}). Accounting for the effect of size is necessary for a precise definition, since aerodynamic lenses are known to focus different particle sizes differently (Zhang et al. 2002, 2004c). The current understanding of particle detection in the AMS indicates that a fraction of low-volatility solid particles such as $(NH_4)_2SO_4$ can also go undetected due to bounce off the vaporizer surface for the current vaporizer design. This gives rise to another collection efficiency term due to particle bounce, for a given particle composition and phase, $E_b(d_{va})$. The overall mass-based total collection efficiency *CE* for the AMS was defined previously as the fraction of the particle mass that is detected compared to what would be detected if the particles were spherical and no particles were lost due to bouncing off the vaporizer (Alfarra et al. 2004). It is very important to note that some particle mass may go undetected because of the limited transmission of the AMS inlet and aerodynamic lens *for spherical particles* at the upper and lower limits of its transmission window. We define here the transmission efficiency of the inlet and lens for spheres as $E_L(d_{va})$. The upper limit of transmission depends on the specific aerodynamic lens being used, but is typically around 1.5 μm, and the particle mass measurement of the AMS is reported as approximately PM_1. $E_s(d_{va})$ is defined relative to $E_L(d_{va})$, so for spheres $E_s(d_{va}) = 1$, even for particles for which $E_L(d_{va}) < 1$. Note that in the absence of other physical effects that lead to particle loss, $CE(d_{va}) = E_L(d_{va}) * E_s(d_{va}) * E_b(d_{va})$ for a given particle size and type. We can also write $CE = E_L * E_s * E_b$ for the total mass. The limitation of the mass-based definition is that it does not explicitly take into account that *CE* due to both shape and bounce effects will depend on particle size, as well as phase. Thus, a different mass-based *CE* may be derived for particles of the same morphology and composition if their size distribution is different. The definitions given here, however, are more precise since they take particle size into account.

Previously, comparisons with other quantitative instruments have been used to derive empirical values of the overall mass-based *CE*. Allan et al. (2004a), Drewnick et al. (2003), and Hogrefe et al. (2004) determined a *CE* of approximately 50% for studies performed in Trinidad Head, CA, New York City, NY, and Whiteface Mountain, NY, which is now believed to have been caused mostly by losses due to the effect of particle bounce at the vaporizer surface (E_b) rather than lens transmission or losses due to focusing effects in the aerodynamic inlet (E_L or E_s respectively). It is preferable to compare the AMS data with that of quantitative instruments using a PM_1 inlet, so that a large uncertainty in E_L due to the particle mass between PM_1 and $PM_{2.5}$ is avoided (Zhang et al. 2004a). Alfarra et al. (2004) present the equations used to calculate mass concentrations from the AMS while taking *CE* into account. *CE* needs to be specified for each AMS measurement, in the AMS data

analysis software, and is currently assumed to depend on the species but not on particle size, although the user can implement the later dependence if this information is available.

2.2. Definition of Non-Sphericity Parameter: Lift Shape Factor

Since spherical particles produce the smallest beam widths after an aerodynamic lens and non-spherical particles result in broader beams, we can define a surrogate non-sphericity parameter, ψ, that we will call the *lift shape factor*, as:

$$\psi_P^{d_{va}} = \frac{\sigma_p^{d_{va}}}{\sigma_{sph}^{d_{va}}} \quad [1]$$

where $\sigma_{sph}^{d_{va}}$ is the beam width (given as standard deviation of the 2D Gaussian distribution) for a sphere of a given vacuum aerodynamic diameter, $\sigma_P^{d_{va}}$ and is the beam width for the particle of interest. It is necessary to compare particles of the same d_{va} since focusing is also known to depend on size (Zhang et al. 2004c). Very little is known at present about the relationship between ψ and the physical particle shape (as determined by microscopy techniques), or between ψ and other parameters capturing the effect of non-sphericity such as the dynamic shape factor χ, or the Jayne shape factor S (DeCarlo et al. 2004). The dynamic shape factor captures the effect of non-sphericity on drag forces on a particle moving in a fluid, and plays a critical role in the interpretation of many particle sizing techniques (DeCarlo et al. 2004).

Only irregular particles experience forces perpendicular to the direction of gas motion ("lift" forces) (Liu et al. 1995a), while for spherical particles lift forces are zero. Given the related physical effects giving rise to χ and ψ (aerodynamic forces and inertia), the ease with which the measurement of ψ can be performed with the beam width probe described here, and the larger difficulty of rigorously determining the dynamic shape factor, future research should explore this relationship as a way to obtain a rapid approximate value for χ in real-time based on the measurement of ψ as a surrogate. The dynamic shape factor depends on the flow regime around the particle, the Reynolds number regime (Stokesian vs. non-Stokesian), and in some cases particle orientation effects (DeCarlo et al. 2004). The lift shape factor will likely depend on the same effects, and may depend on the specific aerodynamic lens design and operating pressure. Some data will be presented in a section below.

2.3. Particle Beam Model

In this section we define a model of the particle density versus position in the beam. In a following section we combine this model with the BWP design to model the attenuation caused by the probe. The particle beam is close to a point source at the exit of the lens (~100 μm diameter, (Heberlein et al. 2001)). Under the high vacuum conditions inside the AMS there are no significant forces, other than a small effect of gravity (DeCarlo et al. 2004) acting on the particles. Thus, we assume that as the particles travel in the vacuum chamber the lateral spread of the particle beam in the direction perpendicular to its travel ("beam width") increases linearly with the distance traveled. Alternatively, the size of a particle beam can be described by the solid angle it fills, arbitrarily defined as the solid angle encompassing a certain fraction of the beam density, such as 90% of the particle concentration (Kane and Johnston 2000), or the beam standard deviation. We will use the latter definition here. The cone defined by the center point of the nozzle at the exit of the lens and the beam dimensions at the vaporizer, having base radius σ, base area A, and height L(the particle flight length) in the limit of small angles will define a solid angle (Serway 1996):

$$\Omega = \frac{A}{L^2} = \frac{\pi\sigma^2}{L^2} \quad [2]$$

which can be rearranged to express the dependence of the beam width on the flight distance as:

$$\sigma = L\sqrt{\frac{\Omega}{\pi}} \quad [3]$$

Note that Equation' (2) is an approximation to the definition of solid angle. It assumes the base of the cone to be a flat circle (of radius σ), whereas the rigorous definition uses the slightly different area of a sector of a sphere (of radius L) on to which the circle is inscribed. All solid angles discussed here are very small, and the error is negligible.

We will use subscripts to specify the position along the AMS particle flight path at which a given σ is defined, e.g., σ_v will refer to the beam width at the AMS vaporizer location. Jayne et al. (2000) showed that for DOP and ammonium nitrate particle beams, the shape of the beam attenuation by a wire, as a function of wire position (x) relative to the center position (x_0) of the beam is well approximated by a 1-D Gaussian distribution with standard deviation σ:

$$g_{1D}(x) = \frac{1}{\sigma\sqrt{2\pi}} \exp\left(-\frac{1}{2}\frac{(x-x_0)^2}{\sigma^2} \right) \quad [4]$$

We revisit this approximation in section 3.3 below.

For our mathematical model we assume that the particle density in the beam can be represented by a 2-D circular Gaussian probability density function (PDF) (Figure 2a). With this assumption, the particle density (i.e., the probability of finding a particle per unit cross sectional area of the beam) is always largest at the center of the beam and decreases monotonically with distance from it, but it does not depend on the azimuthal angle. The equation that describes a 2-D (circular) Gaussian

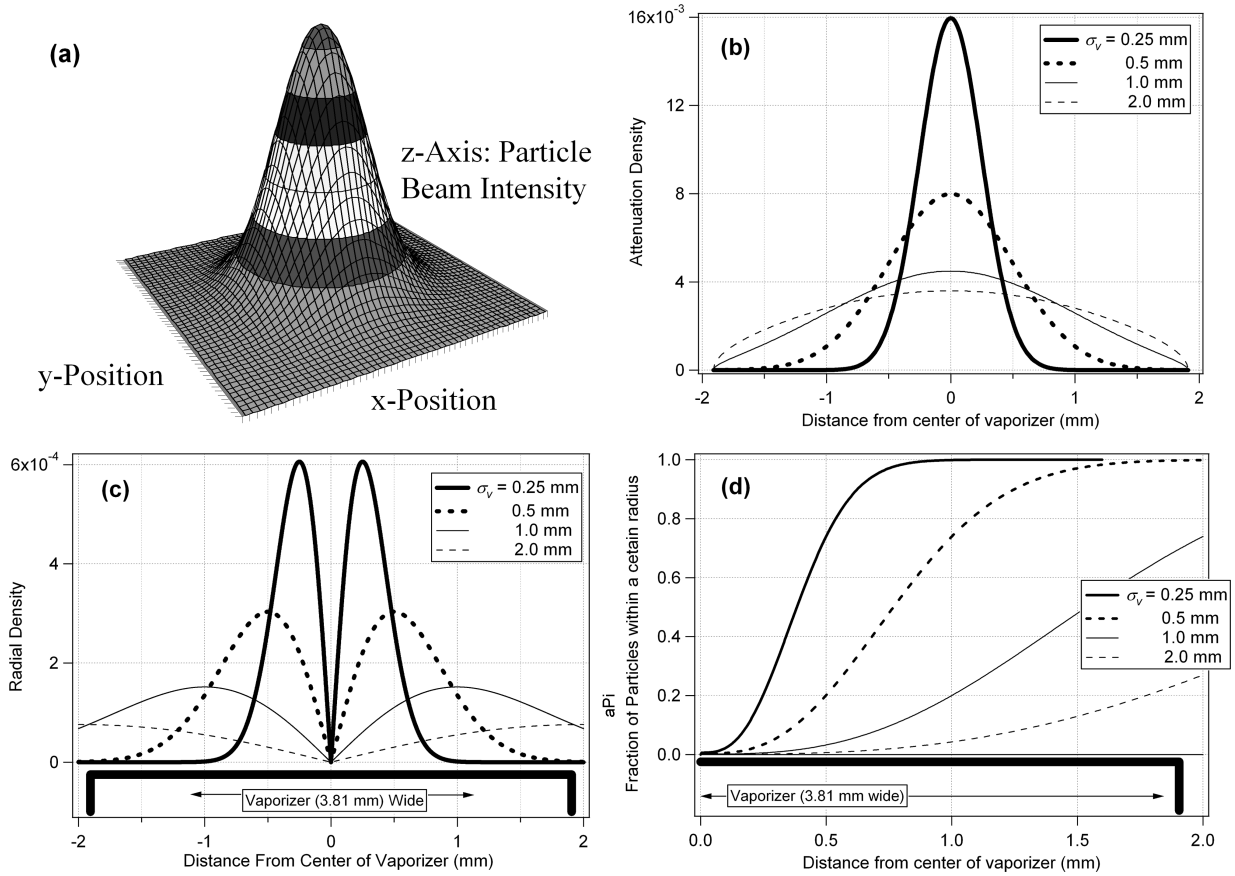

FIG. 2. Physical depiction of a 2-Dimensional Gaussian (2DG) distribution plot. (a) Particle intensity (particles/cm^2) and probability density function (PDF) at any one distance from the lens exit is assumed to follow this 2-D Gaussian, and drop off radially outward from the center axis. (b) *Attenuation density* function, which is the 1-D PDF obtained as the partial integral of the 2-D Gaussian PDF for a given value of x along the y-axis, for all the values of y comprised by the vaporizer. The areas under each curve are normalized to one another. (c) *Radial density* function, which is the 1-D integrated probability-density function (PDF) for all azimuthal angles, θ, around a circle for a 2-D Gaussian distribution. The integrated area under each curve is conserved. (d) Cumulative 1-D PDF (integral between $r = 0$ and a given radius) of the distributions shown in (c). These distributions represent the fraction of the particles that impact the vaporizer at a radial location below a certain value for each particle beam diameter. Note that some curves do not reach unity until beyond the end of the vaporizer for larger beam widths. For a distance equal to the radius of the vaporizer this graph gives directly E_s.

distribution is:

$$g_{2D}(x, y) = \frac{1}{2\pi\sigma^2} \exp\left(-\frac{1}{2} \frac{(x - x_0)^2 + (y - y_0)^2}{\sigma^2} \right) \quad [5]$$

where x and y are the positions along the plane of the distribution, x_0 and y_0 are the coordinates of the center of the distribution in that plane, and σ is the standard deviation. Table 2 shows the fraction of the probability encompassed by 1-D and 2-D Gaussian distributions for different multiples of σ around the center point. Here we will assume that the particle distributions are centered on the axis defined by the lens and the center of the vaporizer (i.e., $x_0 = y_0 = 0$), and thus the only parameter needed to characterize a circular 2-D Gaussian distribution is σ, which we refer to as the particle beam width, and which will depend on the distance from the exit of the lens. We always use the symbol σ with a subscript that identifies the AMS chamber length, and a second subscript for the distance between the lens exit and the position of the beam width measurements.

Figure 2b shows the one-dimensional PDF ($a(x)$) obtained by integrating the 2D distribution along its y-axis, but only for those

TABLE 2
Percentage of the area or volume under 1-D and 2-D Gaussian distributions, respectively, for all independent variable values closer to the mean than different multiples of the standard deviation, σ. 2.35σ ($2 \cdot 1.17\sigma$) corresponds to the full-width-half-maximum value (FWHM) for both 1-D and 2-D Gaussian distributions

	1-D G	2-D G
$\pm 1\sigma$	68.1	47.9
$\pm 1.17\sigma$	75.9	58.1
$\pm 2\sigma$	95.4	91.5
$\pm 3\sigma$	99.7	99.5

values of y that are inside the vaporizer, and renormalizing by the total area so that $a(x)$ is a proper PDF, i.e., $\int_{-r_v}^{r_v} a(x)dx = 1$.

$$a'(x) = \int_{-\sqrt{r_v^2-x^2}}^{\sqrt{r_v^2-x^2}} g_{2D}(x, y)dy \quad [6]$$

$$a(x) = a'(x) \Big/ \int_{-r_v}^{r_v} a'(x)dx \quad [7]$$

where r_v is the radius of the AMS vaporizer ($r_v = 1.905$ mm for the current AMS designs). We will refer to this 1D PDF as the *attenuation density*. Conceptually it can be thought of as the probability density of a particle that would otherwise hit the vaporizer being intercepted for a given value of x and any value of y, as would be obtained with an infinitely thin wire blocking the particle beam along the y direction. The integral of $a(x)$ between two values of x directly yields the probability that a particle will impact the vaporizer between two values of x, or that a particle will be removed from the particle beam by a BWP wire of this width.

Figure 2c shows a different 1D PDF ($b(r)$) which is only a function of the radial coordinate, and that we will refer to as the *radial density*. $b(r)$ is obtained by integrating the volume under the 2D Gaussian curve for all azimuthal angles, θ.

$$b(r) = \int_0^{2\pi} g_{2D}(r, \theta)rd\theta \quad [8]$$

An additional integral of $b(r)$ over the radial coordinate directly yields probabilities, and thus the total area under each curve in the graph is the same, as in the previous case. The area between two radii is the fraction of particles that hit the vaporizer between those two radii for all azimuthal angles θ. Note that the peak in particle radial density is located one σ_v away from the center. Figure 2c also shows that for σ_v values less than 0.5 mm, the radial density drops to very small values before reaching the edge of the AMS vaporizer. This indicates that for particle beams which can be characterized by $\sigma_v < 0.5$ mm (well-focused particles), E_s will be ~100%. Figure 2d is an integration of Figure 2c ($B(R)$), representing the total percentage of particles impacting the vaporizer to the inside of circles with a given radius R.

$$B(R) = \int_0^R b(r)dr \quad [9]$$

Again, for $\sigma_v < 0.5$ mm, all particles will impact the vaporizer, but as σ_v increases, the integrated particle density in the area of the vaporizer can be less than 100%, indicating that the shape-related collection efficiency is below 100%.

While Ω is conserved for a given particle beam under all instrument configurations and particle flight distances, the particle beam width increases linearly with the particle flight distance (Equation 3). The horizontal position of reference (e.g., at the vaporizer, or at the BWP), therefore, must be stated. Since the beam width is the physically meaningful parameter for calculating attenuation by a beam width probe or collection by a vaporizer, we will use this parameter throughout the paper, with subscripts that unequivocally determine the flight distance and thus the relationship between Ω and σ. Table 3 summarizes the four combinations of reference positions and flight lengths. Figure 1 shows a graphical representation of these positions, and Table 1 lists the relevant distances. In the remainder of the paper, unless otherwise stated, all discussion will be referenced to the plane of the vaporizer, and will refer to the 255-series "long" AMS particle flight length ($L_l = 450$ mm). We will use two parameters to characterize the beam: the solid angle of the beam, Ω (in steradians) and the beam width at the vaporizer σ_{lv} (in mm), where the subscript l refers to the "long" chamber, and v references the plane of the vaporizer. σ_{lw} is the particle beam width in the plane of the BWP for the long chamber, while σ_{sv} and σ_{sw} are the equivalent definitions for the AMS short chamber.

TABLE 3
Notation for beam width, σ, must be referenced to a particular particle flight length (AMS chamber configuration) and plane of reference in order to be meaningful. The table defines the four combinations used in this paper

	AMS Chamber configuration	
	Long	Short
Plane of reference		
BWP (wire)	σ_{lw}	σ_{sw}
Vaporizer	σ_{lv}	σ_{sv}

Note that the 2-D Gaussian assumption would fail if the lens is not well-aligned, and particles are lost via impaction with one of the skimmers inside the instrument. Under these conditions (arising from user error) the shape of the beam could be very different from that predicted by the model. Also note that the total flight length in the AMS is different from the flight length used in the AMS calibration of particle velocity vs. particle size (Jayne et al. 2000). The latter is the distance from the particle chopper to the vaporizer (395 mm), since that is the length that corresponds to the measured particle time-of-flight, rather than from the lens exit to the vaporizer.

2.4. Beam Width Probe Design

A beam width probe was designed and implemented to provide a real-time quantitative measurement of the width of the particle beam in the AMS, and thus enable the estimation of ψ and E_s for the particles being sampled. Figure 3 shows a schematic diagram of the probe set-up together with the vaporizer from two different perspectives. Two probes have been developed. The first prototype uses a servo motor (HiTech, HS-81)

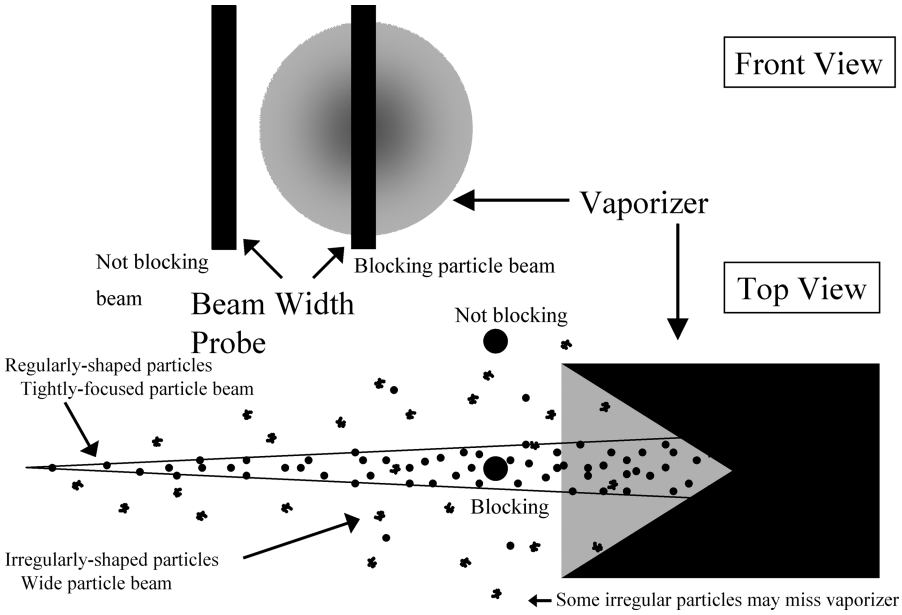

FIG. 3. Schematic diagram of the beam-width probe from two perpendicular views. The particle beam is projected from the lens exit towards the vaporizer, and it broadens as it moves down the vacuum chamber. Particles will ideally follow a narrow trajectory (spherical particles) and impact the vaporizer. Some particles may follow trajectories that will miss the vaporizer surface (irregular shapes). The beam width probe is positioned selectively in positions that either partially block particles moving towards the vaporizer, or in the 'out' position to obtain un-attenuated measurements. This diagram is not drawn to scale.

to position the probe (a wire or ribbon of known dimension) across the path of the particle beam. The servo device has a position resolution of ~90 μm. A second, more precise device utilizing a stepper motor (HSI Inc., LC1574W-05) was built for improved resolution (20 μm). The BWP is mounted at the end of the particle time-of-flight chamber and near the vaporizer (actual distances shown in Figure 1). When the probe is positioned outside the particle beam, or outside the vaporizer, no signal attenuation results. As the probe is moved to a position in which it blocks part of the particle beam and vaporizer, some incoming particles are prevented from reaching the vaporizer. The AMS signal, which is proportional to the total particle mass for each chemical component, is reduced proportionally. Because the particle time-of-flight region where the probe is located is under vacuum (approximately 10^{-3} Pa) there are very few collisions with gas molecules (mean free path between collisions between a 100-nm particle and gas molecules is approximately $\lambda \sim 1$ m) (Zhang 2004), and particles travel in straight lines (neglecting gravity). Thus, particles whose trajectories are intercepted by the probe will not reach the vaporizer. Thus, the BWP shades a certain fraction of the vaporizer and reduces the AMS signal by the fraction of particles in this shaded area. The BWP has also become very useful for determining alignment of the lens. Instead of moving the lens slowly back and forth, and watching for a resultant drop in signal when the beam was pushed beyond the sides of vaporizer, the BWP can be quickly moved back and forth to determine the horizontal placement of the particle beam focus. With the current BWP design, however, this works only in the horizontal direction. For vertical alignment the BWP needs to be rotated 90 degrees, which requires breaking the vacuum, or the "classical" alignment procedure by lens aiming is still necessary.

2.5. Beam Width Probe Model

By precisely stepping the wire probe across the particle beam at regular intervals as described above, and recording the AMS signal as a function of probe position, the attenuation of the beam can be mapped. For a given wire diameter (d_w), 2-D Gaussian particle beams of different widths will produce unique attenuation versus probe position curves. To aid in the design of an optimal probe and in the interpretation of experimental data, a model was implemented to calculate the shape of the particle transmission curve as a function of wire position, wire diameter and particle beam width. The model assumes that the particle beam density as a function of radial position is well represented by a circular two-dimensional Gaussian distribution, as described above. The model is computed in two steps. First the vaporizer is discretized along the x-axis, and the integral of the particle beam density function for a small interval of x and all values of y *inside the vaporizer* (the "attenuation density" described above, $a(x)$, see Equation 7) are calculated for a series of particle beam widths. The attenuation created by a given wire as it is set to block certain x positions is just the integral of the attenuation density of the blocked x positions, since the attenuation density is a PDF. Note that the total detectable signal could be smaller than the total beam intensity if $E_s < 100\%$ (i.e., beam width > diameter of the vaporizer).

2.6. Field Operation of the BWP

For normal operation of the probe during a field or laboratory study, several wire positions are chosen, e.g., eight total steps, including the center, three on each side of the center (but within the vaporizer cross section, "partially blocking" positions), and one position completely outside of the vaporizer ("out" position). The probe is moved to each successive position in one direction, with the "out" position interleaved in time between each "partially blocking" position. Data taken during the periods when the probe is completely outside the beam and no attenuation occurs allows for a total mass trend to be established for ambient monitoring and comparison with other instrumentation. The number of positions should be chosen to provide enough attenuation, measured as a function of wire position, to constrain the data fit to the model curves. In practice it has been determined that using seven "blocking" steps, with the interleaved "unblocking" position is sufficient. The one-position cycle time (out → partially blocking → out) must be shorter than the time scale of most changes in the particle concentrations sampled, so that the ratio of the attenuated signal to the average of the unattenuated signals before and after it is correct. In addition, the total cycle time (loop through an entire round of positions) must be shorter than the time scale of changes in the nature of the particle population, so that the beam attenuation profile constructed from different positions is meaningful.

Under normal ground-based field campaign operation, the beam width probe is often configured to take data in seven partially blocking positions at full wire steps. For example, this would correspond to a step every 0.5 mm for a 0.5 mm wire, with the middle of the probe positioned at: −1.5, −1.0, −0.5, 0, 0.5, 1.0, and 1.5 mm relative to the vaporizer center. This longitudinally covers the center 3.5 mm of the vaporizer, and contains most of the information. Using seven steps, interleaved with seven non-blocking positions amounts to a 14-minute cycle with 1-minute averaging at each position. For applications when time resolution is critical, such as when sampling from aircraft, it is recommended that only two positions (center and non-blocking) will be selected and applied with a small duty cycle (∼10% of the time in the blocking position) in conjunction with the new "Jump Mass Spectrum" mode (i.e., selective ion monitoring) of the AMS, so as to minimize the loss of normal mode data and maximize the temporal resolution of the ψ and E_s determinations.

3. RESULTS AND DISCUSSION

3.1. Particle Collection Efficiency

The vaporizer diameter and its distance from the lens exit define a cone of a certain solid angle. For the long-chamber AMS length of 450 mm from lens exit to vaporizer, the solid angle of collection is 5.63×10^{-5} sr (Table 1). Provided that the center of the particle beam is centered on the vaporizer, particles that follow a trajectory within this cone will impact the vaporizer. At this position the relative number of particles (probability density) at each location radially outward from the beam center, and therefore at each solid angle, is only a function of the particle beam width at the vaporizer (σ_v). The vaporizer collection efficiency due to shape (E_s) is then simply a function of the particle beam width at the vaporizer relative to the vaporizer diameter, or alternatively of the solid angle that describes the beam (Ω_{beam}) compared to the vaporizer solid angle ($\Omega_{collection}$). Figure 4 shows E_s versus σ_v, and vs. Ω_{beam} calculated with the

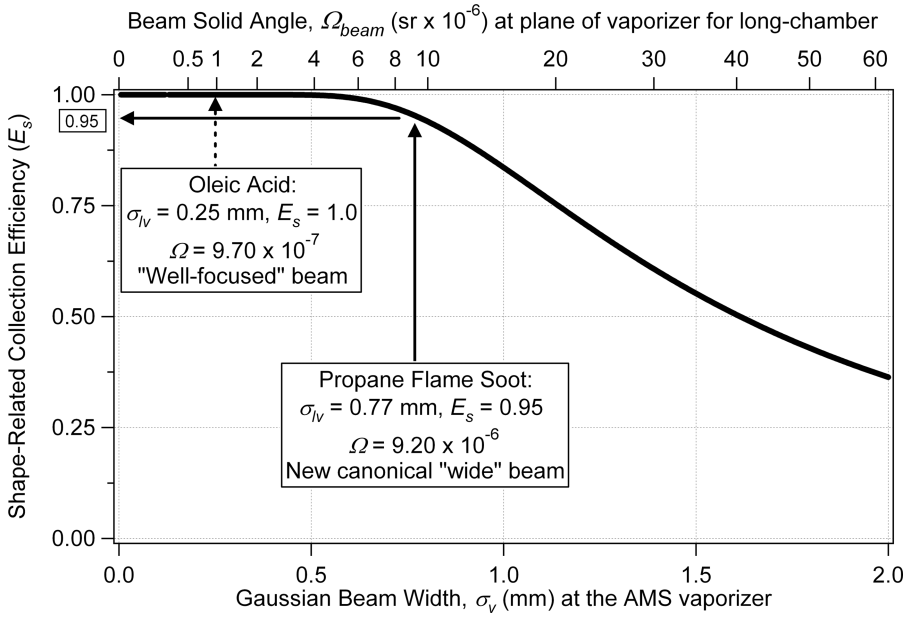

FIG. 4. Variation of the collection efficiency due to shape (E_s) as a function of the width of the particle beam at the vaporizer (beam standard deviation, σ_{lv}) on the bottom axis, and beam solid angle (Ω_{beam}) on the top axis. The experimentally determined beam widths and calculated E_s for spherical particles (well-focused, oleic acid) and very irregular (poorly-focused, flame soot) particles are marked.

2-D Gaussian model described above. The curve vs. σ_v is the same for all chamber lengths, provided that the correct beam width at the vaporizer is used. Beam widths measured at different flight lengths or in different chambers must first be scaled using Equation 3.

E_s remains 100% for narrow beams (small σ_v), and until the beam becomes wide enough so that a significant fraction of its tail misses the vaporizer surface. At $\sigma_v \sim 0.625$ mm ($\Omega \sim 5.63 \times 10^{-5}$ sr for the AMS long chamber) E_s drops below 99%. For very irregular soot particles that have a $\sigma_{lv} =$ 0.77 mm (Slowik et al. 2004) E_s will be approximately 95% for the AMS long chamber. Reducing the chamber length by 10 cm would reduce the beam width at the vaporizer, σ_{sv} to 0.59 mm, and thus increase E_s for these less well focused soot particles to slightly more than 99%. Partially as a consequence of these results, Aerodyne Research has produced a chamber with a particle flight path approximately 10 cm shorter (referred to here as the "short" chamber, 215-series design). This increase in E_s can be accomplished with less than proportional loss in particle size resolution (Jimenez et al. 2001). As the particle flight length decreases, the time-of-flight for the largest particle to be sampled by the AMS in a given experiment ($d_{\max}$) also decreases. This allows the increase of the chopper frequency so that a chopper period still allows a particle with $d_{va} = d_{\max}$ to arrive before the start of the next chopper cycle. The increased chopper frequency reduces the chopper opening time, which is one of the major uncertainties in particle time-of-flight (PToF) that limits the AMS size resolution, and thus this relative uncertainty stays constant. The other major uncertainty in PToF that limits the size resolution of the AMS is particle vaporization time (τ_{vap}). Since τ_{vap} is constant and does not depend on chamber length or chopper parameters, it will represent a proportionally larger uncertainty of the total PToF, which does lead to some decrease in AMS size resolution.

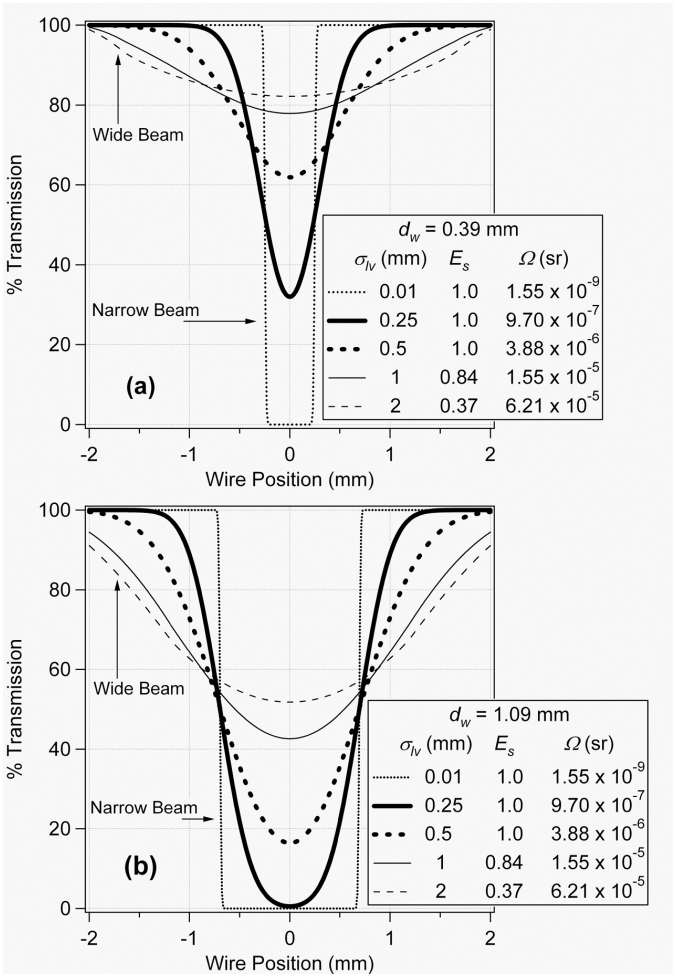

FIG. 5. (a) Particle beam transmission curves for a BWP with a 0.39 mm wire (nearly optimal for well-focused beams) for the long AMS chamber. The different lines show the attenuation of particle beam vs. BWP position for several particle beam widths (σ_{lv}). (b) Similar curves for a 1.09 mm wire probe, showing broader and deeper attenuation for each particle beam width. This wire is optimal for laboratory-generated flame soot particles (in the long AMS chamber), which are used here as a surrogate for poorly focused beams.

3.2. Beam Width Probe Model Results

Throughout the discussion of these model results, a range of reasonably expected beam widths has been used. The lower bound was defined by the spherical particles with the tightest focus, as determined by the laboratory studies discussed in a following section. Liquid oleic acid particles with mean d_{va} of 320 nm show $\sigma_{lv} = 0.13$ mm. Slowik et al. (2004) show that very irregular soot particles generated by a propane flame burner have $\sigma_{lv} = 0.77$ mm, defining the upper bound of expected beam widths. Figures 5a and 5b show the modeled results of the particle beam attenuation versus probe position for probe diameters of 0.39 mm and 1.09 mm, which will be shown later to be the optimal probes for the above-defined canonical narrow and wide beams, respectively. Again, all results presented refer to the "long" AMS chamber. Each curve shows the percentage beam transmission (normalized to an unattenuated beam) as the probe is moved across to block a fraction of the vaporizer. For an extremely narrow beam ($\sigma_{lv} = 0.01$ mm), particle beam attenuation is predicted only when the wire intersects the center of the vaporizer, where the beam is focused, using probes of the above mentioned diameters. Note that this beam width is unrealistically small given current aerodynamic lens technology, as the lowest beam widths for spherical particles for this flight length are of the order of $\sigma_{lv} = 0.13 - 0.25$ mm. The limit of a very narrow beam is shown in Figure 5, however, because it provides an asymptotic result and helps in understanding the results of the model. The width of the attenuated section is simply the width of the wire as projected onto the vaporizer plane. Note that the "shadow" of the wire broadens slightly due to the constancy of the solid angle, as defined earlier (Equation 3).

For an extremely broad (nearly uniform) beam of particles the attenuation is simply the geometric area of the vaporizer that the wire probe is blocking (because the particle probability

density is nearly uniform across the width of the vaporizer). For particle beam widths of intermediate values and realistic proportion, the percentage of particles blocked is the product of the geometric area the probe shadow casts on the vaporizer with the relative concentration of particles (the probability density given by the Gaussian distribution) for those locations. For a given geometry and wire diameter, each beam width gives rise to a unique attenuation curve. Optimal probe geometries will be discussed below.

3.3. Parameterization of the Model Results

Once data has been acquired at a number of wire steps, it can be plotted as a function of wire position, and interpreted by one of two different methods. To most rigorously determine the width of the beam, and therefore collection and shape information, the data should be plotted alongside modeled BWP curves, as done in Figure 5. With this method, the location of the center of the beam (x_0) is fitted (see below) and input to the model calculation, which then produces curves for a number of beam width values. The model output model curve that returns the minimal chi-squared value when compared with the input data determines the optimal beam width value.

In many cases, however, a 1-D Gaussian curve captures most of the variation in the detailed experimental results (Jayne et al. 2000). So for faster and easier analysis, the seven data points can be fit to a one-dimensional Gaussian function (Equation 4). This "1DG" parameterization achieves two benefits: (1) experimental data can be easily and quickly analyzed inter-compared based on σ_{1DG}, the standard deviation of the 1DG fit curve, for first-order data analysis, and (2) imperfections in the lens alignment can be removed from BWP analysis, because the Gaussian fit will automatically "re-center" the data to a better estimate of the true horizontal beam center, which in general will not be exactly the same as the vaporizer center. This re-centering can be used to define a horizontal offset of the beam center for the modeling of σ_{lv} for misaligned particle beams. Figure 6 shows the relationship between σ_{lv} and σ_{1DG} for four different BWP diameters. For $\sigma_{lv} > d_w/2$, σ_{1DG} is a reasonable approximation to σ_{lv}. This rule of thumb allows a quick first-order analysis and inter-comparison of experimental data. Note that the validity of the 2DG assumption is not directly related to the results of the 1DG fit. The validity of the 1DG parameterization is further discussed in the probe optimization section below.

3.4. Model Verification and Comparison with Experimental Data

We performed laboratory experiments using a short-chamber AMS to test the assumption that the particle beam can be approximated by a 2-D Gaussian distribution. Beam width data for monodisperse particles were acquired by first generating pure-species polydisperse particle distributions using a Collision atomizer (TSI model 3076, St. Paul, MN), and then size-selecting particles with a differential mobility analyzer (DMA, TSI model 3081, St. Paul, MN). All solutions were prepared by dissolving the species in HPLC-grade water, with the exception that oleic acid was dissolved in HPLC-grade ethanol. The aerosol was dried by three silica-gel diffusion driers in series, and the humidity after the driers was monitored with a relative humidity probe (Vaisala Humitter 50Y, Helsinki, Finland). RH was kept under 25% throughout all experiments. Then the aerosol was introduced into the AMS inlet, where the particles were focused onto a narrow beam that was directed onto the AMS vaporizer. The beam width was measured as the BWP was walked across the vaporizer in very small steps (22 total positions).

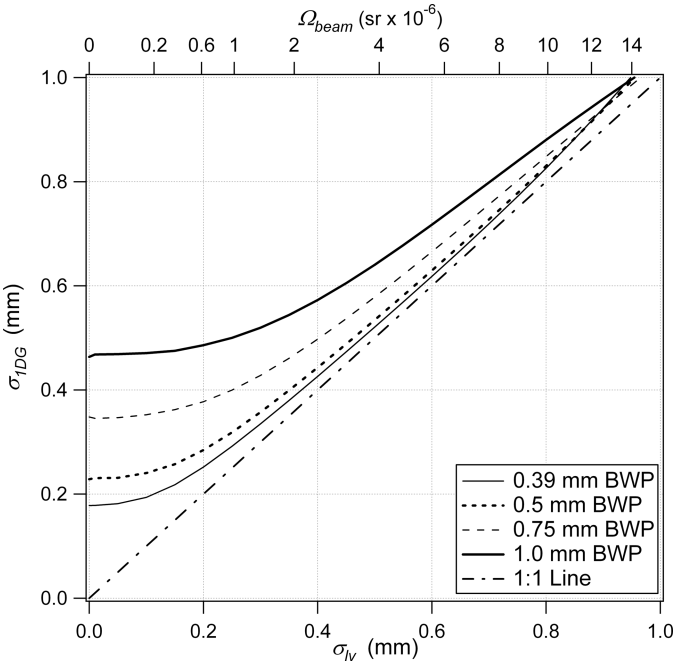

FIG. 6. Relationship between the beam width approximated by a 1-dimensional Gaussian data fit (σ_{1DG}) and the more rigorous value of beam width determined by the model output (σ_{lv}) for four BWP sizes. Note that when using Igor Pro (Wavemetrics, Inc.) the Gaussian fit "width" parameter returned is $\frac{\sqrt{2}}{2}\sigma_{1DG}$.

Analysis was performed using the signal from species-dependent fragment ions (NH_4NO_3: *m/z* 16, 17, 30, and 46; $(NH_4)_2SO_4$: *m/z* 16, 17, 48, and 64; Oleic Acid: *m/z* 43 and 57) from singly-charged particles exiting the DMA, with the exception that 550 nm oleic acid data were taken from doubly-charged particles and using only *m/z* 43. Two monodisperse sizes were used for each species, approximately 110 nm and 320 nm, in addition to 550 nm oleic acid. Particle transmission plots for these data are shown in Figure 7. The beam profiles of all species and particle sizes are reasonably well captured by the results of the BWP computer model described above, which indicates that the two-dimensional circular Gaussian approximation for the particle probability density is reasonable. Note that the particle beam focus points with a real lens are slightly size-dependent, due to imperfections in lens machining.

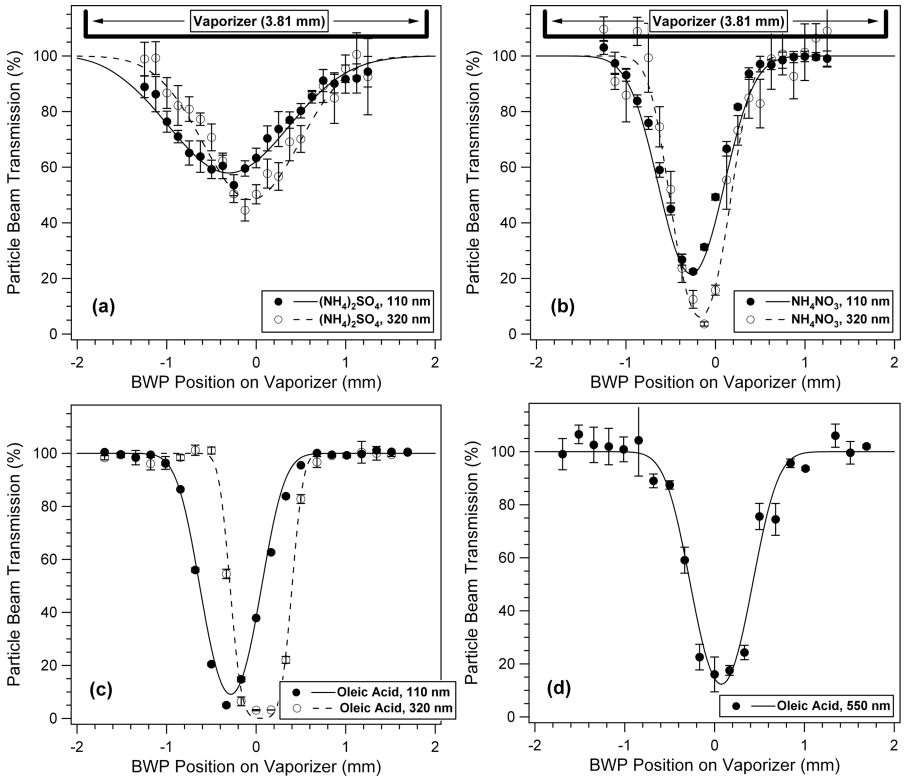

FIG. 7. Pure, monodisperse particle beam profiles, shown ± the standard error of the mean. Data were acquired with a "short" chamber, equipped with a high-throughput lens sampling from 640 torr (850 hPa; flow rate = 2.3 std cm^3 s^{-1}) with a 0.5 mm wire probe. 21 BWP positions were used to cover the surface of the vaporizer with high spatial resolution. Signal was averaged for about 1 minute in each position. σ_{lv} and Ω values for these were determined using the BWP model discussed in this work, and are listed in Table 4. Symbols show experimental data, and curves show model outputs fit to the data. (a) BWP profiles for $(NH_4)_2SO_4$ particles, $d_{va} = 110$ nm, (b) NH_4NO_3 particles, (c) Oleic Acid particles of mean $d_{va} = 110$, 320 nm, and (d) Oleic Acid particles of mean $d_{va} = 550$ nm.

The beam widths and solid angles derived from the fits of the lab-generated particles (where $E_L = 1$) are given in Table 4. The table also provides a review of particle beam width measurements presented in publications from a number of other research groups. Each group performed beam width analysis by different means, and these data were all converted to estimated σ_{lv}. Most measurements report comparable beam widths, and perfect agreement is not expected, since slightly different lens designs and operating pressures were used in each study. Figure 8a is a histogram of the summarized beam width values. The two Schreiner et al. papers (1999; 1998) use a different lens design that operates at much higher pressures with much smaller lens orifices. This results in different particle focusing, and for this reason the Schreiner data have been plotted on the right axis with a different range. The papers using Liu-style lenses have been divided into spherical particles (sorted by size), left, and non-spherical particles (sorted by species), center. Note that Katrib et al. (2005) showed PSLs to be slightly non-spherical. This shows that spherical particles appear to have size-dependent focusing, as expected. Very small particles (40 nm) produce broad beams due to the limitations in the focusing of the aerodynamic lens and as a result of particle Brownian motion. Large particles (>500 nm) do not focus very well due to their high inertia, with the consequence that particles only partially follow the gas streamlines in the lens that causes the particle focusing. Intermediate sizes of spherical particles (300 nm) show optimal focusing (Zhang et al. 2004c). Non-spherical particles are generally less well focused than spherical ones, and focusing is different for the various species (due to their different shapes).

Figure 8b relates this shape information as the lift-shape factor, ψ, introduced here (Equation 1) and showing the effect of shape on particle focusing. Each non-spherical data point from Figure 8a was referenced to a corresponding spherical data point of similar size from the same publication. Su et al. (2004) did not record a spherical data point, and so the average of the 130-nm data points from Katrib et al. (2005) was used for reference. Slowik et al (2004) also did not record a spherical data point, and so the 320-nm Oleic Acid point from this work was used.

The precise position of the horizontal center of the particle beam can be particle size-dependent due to imperfections in the lens construction. This was observed in the particle time of flight data when a polydisperse, dry ammonium nitrate aerosol was blocked with a 0.5 mm wire in various horizontal positions. The horizontal position of the beam center at each size reversed

TABLE 4
A summary of particle beam width measurements published by several research groups, and those from this work. Since each group presents results in a different format and for different particle flight distances, the reported values have all been scaled to the standard deviation of a Gaussian beam at the particle flight distance of the long-chamber AMS (450 mm), and to the solid angle that this area would encompass. Note that the lens types used for AMS instruments are similar, but not identical to the Liu et al. lens. Ψ has also been calculated when appropriate, as described in the text

Citation	Lens Type	Lens P (torr)	Particle Species	Particle Size (nm)	Flight Dist. (mm)	σ_{lv} (mm)	Ψ	Solid Angle (sr)
Liu 1995b	Liu	0.35-0.7	DOS	40	430	**0.9**	-	**1.1×10^{-5}**
			DOS	230		**0.12**	-	**2.3×10^{-7}**
Schreiner 1998	Schreiner	37.5	DOS		95	**2.7**	-	**1.1×10^{-4}**
Schreiner 1999	Schreiner	15	DEHS	700	87	**0.5**	-	**4.4×10^{-6}**
			DEHS	1150		**0.5**	-	**4.4×10^{-6}**
			NaCl	190-480		**2.3**	**4.36**	**8.4×10^{-5}**
			NaCl	300-850		**3.4**	**6.27**	**1.7×10^{-4}**
Jayne 2000	Liu	2.1	DOP	350	160	**0.15**	-	**3.7×10^{-7}**
			NH_4NO_3	350		**0.27**	**1.77**	**1.2×10^{-6}**
Kane 2001	Liu	2	Oleic	200	250	**0.22**	-	**7.5×10^{-7}**
			NBA	poly		**0.51**	-	**4.0×10^{-6}**
			NaCl	poly		**1.08**	**4.91**	**1.8×10^{-5}**
Katrib 2005	Liu	2.1	Coated PSL	111	450	**0.3**	-	**1.4×10^{-6}**
			$NaCl_{(aq)}$	130		**0.29**	-	**1.3×10^{-6}**
			Oleic	130		**0.32**	-	**1.5×10^{-6}**
			Unreact. Oleic	130		**0.24**	-	**8.9×10^{-7}**
			React. Oleic	130		**0.26**	-	**1.0×10^{-6}**
			NaCl	100		**0.47**	**1.60**	**3.5×10^{-6}**
			PSL	107		**0.39**	**1.31**	**2.3×10^{-6}**
			$NaCl_{(s)}$	130		**0.61**	**2.16**	**5.7×10^{-6}**
Slowik 2004	Liu	2	Flame Soot	350	325	**0.77**	**5.95**	**9.2×10^{-6}**
Su 2004	Liu	2.1	PSL	100	200	**0.32**	**1.16**	**1.6×10^{-6}**
			PSL	120		**0.34**	**1.23**	**1.8×10^{-6}**
			PSL	170		**0.32**	**1.16**	**1.6×10^{-6}**
			PSL	290		**0.36**	**1.29**	**2.0×10^{-6}**
Huffman 2005	Liu	2.1	Oleic	110	348	**0.27**	-	**1.1×10^{-6}**
			Oleic	320		**0.13**	-	**2.6×10^{-7}**
			Oleic	550		**0.29**	-	**1.3×10^{-6}**
			NH_4NO_3	110		**0.36**	**1.37**	**2.0×10^{-6}**
			NH_4NO_3	320		**0.24**	**1.85**	**8.9×10^{-7}**
			$(NH_4)_2SO_4$	110		**0.82**	**3.1**	**1.0×10^{-5}**
			$(NH_4)_2SO_4$	320		**0.64**	**4.95**	**6.4×10^{-6}**

when the lens was rotated 180 degrees, indicating that the particle beam focus rotated with the lens (Middlebrook and Matthew 2004). This understanding that beam focus is size-dependent partially explains why the particle beam width of polydisperse beams is larger than expected, and why monodisperse particles must be chosen for beam width and lift shape factor studies.

Computer code for rigorously analyzing laboratory and field data using the 2-dimensional model is available at: http://cires.colorado.edu/jimenez-group/SI/.

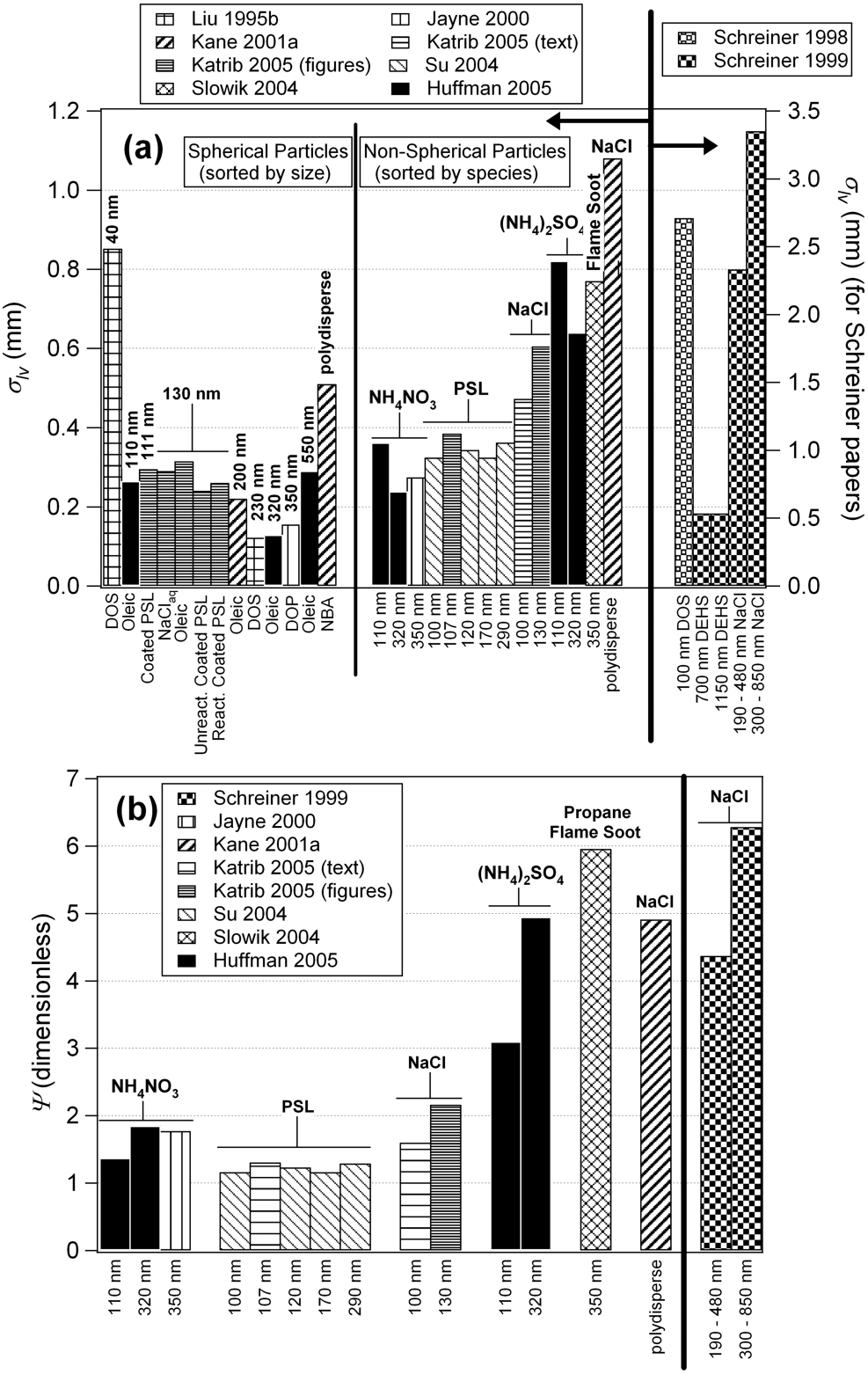

FIG. 8. (a) Literature summary of beam width measurements from a number of research groups. Note that the Schreiner papers employ a high-pressure lens, and have been plotted on the right axis. These lenses may focus particles differently than the ones described in the other five papers, which all use the Liu-style lens (left axis). Data from instruments using the Liu lens are divided into mostly spherical particle types (left group) sorted by size, and non-spherical particles (center group) sorted by species. The Katrib 2005 data was taken from textual references of beam width data, as well as from Figure 2 of that paper, which was then analyzed via the methods described in this paper. Note that PSLs are considered slightly non-spherical based on the results of Katrib et al. (2005). (b) Ψ values have been calculated for corresponding beam width data. Each non-spherical particle σ_{lv} was divided by the σ_{lv} for a spherical particle of similar size, from the same publication.

3.5. Field Results

Allan et al. (2004) suggest that some ambient non-spherical particles may also be collected with less than 100% efficiency by the AMS. Although this effect was previously attributed to very wide ambient particle beams, it has recently been shown that most of the reduced particle collection efficiency is due, rather, to particle bounce at the vaporizer (Onasch 2004). With the results of the model discussed here, it is now believed that reduced collection of ambient particles due to very wide particle beams is not a significant problem for the AMS. Salcedo et al. (2005), Weimer et al. (2005) and Delia (2004) all conclude that $E_s \sim 1$ for ambient particles studied in the field in Mexico City, New York City, and Duke Forest, North Carolina respectively.

3.6. Optimization of the Wire Probe Width

The BWP can be used to measure the particle beam width and estimate the lift shape factor (ψ) and shape-related collection efficiency (E_s) in near real time. By running the model for a variety of BWP dimensions (diameters, d_w), we can determine optimal probe dimensions with maximum sensitivity to measure E_s or ψ (i.e., to have the lowest possible uncertainty on the measured E_s or ψ). The optimum wire width will depend on the width of the beam under study, and thus a compromise should be made, since the probe is inside the vacuum chamber and cannot be changed quickly under varying ambient conditions.

For successively thicker probes and a given beam width, the signal attenuation at each point increases, and the transmission at the center position drops. In order to provide a precise beam width (σ_{lv}) measurement, the sensitivity (S_σ), which is the change in attenuation of the AMS signal relative to a change in beam width, has to be maximized. S_σ is defined as:

$$S_\sigma = \frac{da_c}{d\sigma} \qquad [10]$$

and has units of inverse length (mm^{-1}), where a_c is the beam attenuation at the central probe position.

The precise measurement of E_s requires optimizing the sensitivity of the attenuation signal with respect to that parameter (S_{Es}), which is defined as:

$$S_{E_s} = \frac{da_c}{dE_S} \qquad [11]$$

and is dimensionless. Conceptually, maximizing S_σ by choosing the optimum d_w is equivalent to maximizing the separation between the curves, such as those in Figure 5, representing the differences in attenuation caused by small changes in σ_{lv}. For discussion of the wire optimization towards narrow beams, a beam width of 0.25 mm was chosen to represent reasonably well focused, nearly spherical particles. While the value of $\sigma_{lv} = 0.13$ mm was shown to be optimal for the particles exhibiting the best possible focus (Figure 7), the larger value is more realistic for well-focused ambient particles, and has been taken as the approximate average of the spherical data points from other studies (Figure 8a). Note that E_s remains unity in each case.

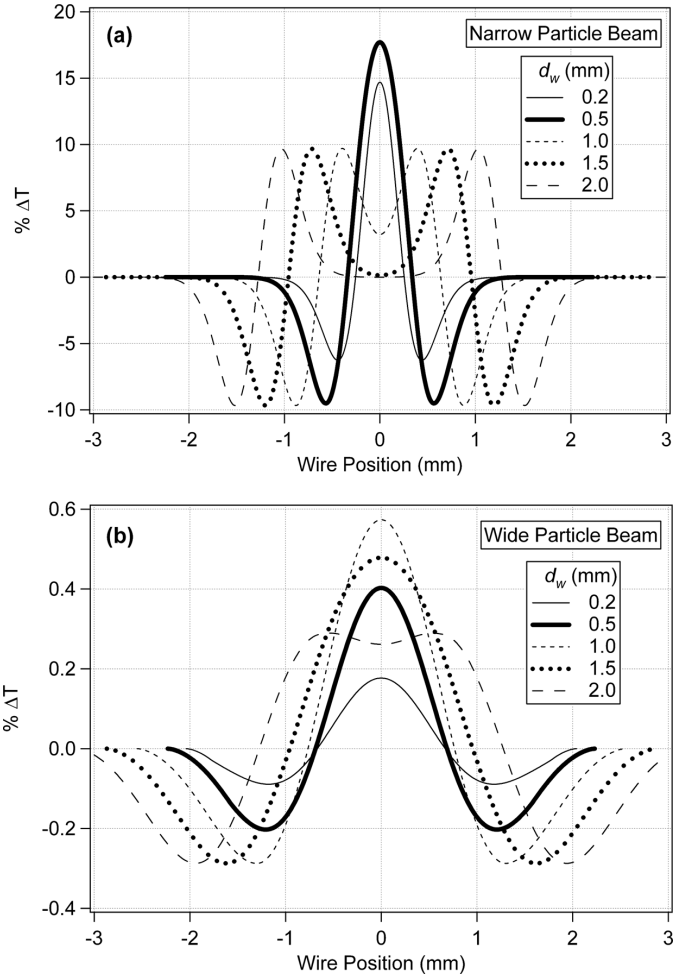

FIG. 9. Difference curves between the modeled transmission curves (similar to Figure 5) for two close particle beam widths for a variety of probe diameters. The difference from zero in these plots is proportional to the sensitivity of the beam width measurement for each wire probe size and radial position. (a) Difference curves between $\sigma_{lv} = 0.22$ mm and 0.23 mm, which characterize the sensitivity towards well-focused beams. (b) Difference curves between $\sigma_{lv} = 0.70$ mm and 0.71 mm representing the sensitivity towards poorly-focused beams. The maximum sensitivity is found at the center, except when $d_w \gg \sigma_{lv}$.

The first step in this approach is illustrated in Figure 9, which shows the difference between two close values of σ_{lv} for several d_w. Examples for narrow and wide particle beams are shown in Figures 9a and 9b, respectively. The absolute value of the "difference curves" in the plot describes how far the two absolute attenuation curves (as in Figure 5a) are separated from one another, and therefore how much sensitivity is achieved at each of the probe positions. The center position has the largest sensitivity for most cases, but as d_w/σ_{lv} increases, the point of maximum sensitivity moves away from the center and towards

the vaporizer edges. We will focus on the attenuation at the center position for the rest of this analysis, since this position will have the maximum attenuation for most cases of interest.

The mathematical procedure for estimating the sensitivity is summarized in Figure 10a. Figure 10a shows $da_c/d\sigma_{lv}$, $d\sigma_{lv}/dE_s$, and da_c/dE_s for $d_w = 0.5$ mm. $da_c/d\sigma_{lv}$ was calculated directly from the model by computing the difference curves (as in Fig. 9) in small $\Delta\sigma_{lv}$ intervals (for a given d_w), and then estimating the derivative numerically as $\Delta a_c/\Delta\sigma_{lv}$. This particular wire ($d_w = 0.5$ mm) is most sensitive for the measurement of beam width around $\sigma_{lv} \approx 0.23$ mm, but maintains some sensitivity for much larger beam widths. The sensitivity to E_s can be computed by using the following mathematical relationship:

$$\frac{da_c}{dE_S} = \frac{da_c}{d\sigma_{lv}} \times \frac{d\sigma_{lv}}{dE_S} \qquad [12]$$

The term $d\sigma_{lv}/dE_s$ can be easily computed as the numerical approximation to the derivative of the curve in Figure 4.

Figure 10b summarizes S_σ for all particle beam and wire probe diameters. An optimal d_w can be chosen for every σ_{lv}, but there is a range of d_w that provides significant sensitivity for a given σ_{lv}. Curves joining the points of maximum S_σ with respect to σ_{lv} and d_w are shown in the figure. The line of maximum sensitivity with respect to d_w ($S_{\sigma(max,d)}$) was calculated by conceptually "slicing" the plot in the horizontal direction, and plotting the maximum ridge-line, while the maximum with respect to σ_{lv} ($S_{\sigma(max,\sigma)}$) was calculated by slicing the plot in the vertical direction. This means that due to the slope and orientation of the 3D ridgeline on the plot, for a given σ_{lv}, an optimal d_w can be chosen, but that this d_w may also be more sensitive to a different σ_{lv}. A linear approximation of $d_{wl,opt} = 1.55{\cdot}\sigma_{lv}$ holds well for $\sigma_{lv} < 0.6$ mm, while for larger σ_{lv} the line over-estimates the optimal d_w. The optimum wire for measuring small differences between nearly spherical particles producing narrow beams ($\sigma_{lv} \sim 0.25$ mm) is $d_w \sim 0.39$ mm while for a wide beam such as that produced by fractal soot ($\sigma_{lv} \sim 0.77$ mm) the optimum wire is $d_w \sim 1.09$ mm. A $d_w \sim 0.6$ mm provides reasonable sensitivity over the expected range of beam widths for ambient studies.

Figure 10c shows the sensitivity to E_s (S_{Es}). Note that $E_s > 0.99$ until $\sigma_{lv} > 0.625$ mm. For smaller σ_{lv} the term $d\sigma_s/dE_s$ in Equation 12 can be very large since E_s changes very little as σ_{lv} changes, resulting in very large values of da/dE_s. However, these have no practical significance since $E_s \sim 1$, and thus they are not shown in the figure. For $\sigma_{lv} > 0.625$ mm there is an optimum d_w for determining E_s (maximum S_{Es}). The curve of maximum S_σ is the same as the curve of maximum S_{Es}, because the two sensitivities are related by a factor that does not depend on σ_{lv} (Equation 12).

Figure 11 provides an alternative representation for the information provided by the BWP, which can be especially useful to guide in choosing the additional probe positions (other than the center) to be used for field studies. Figure 11a uses $d_w = 1.0$ mm,

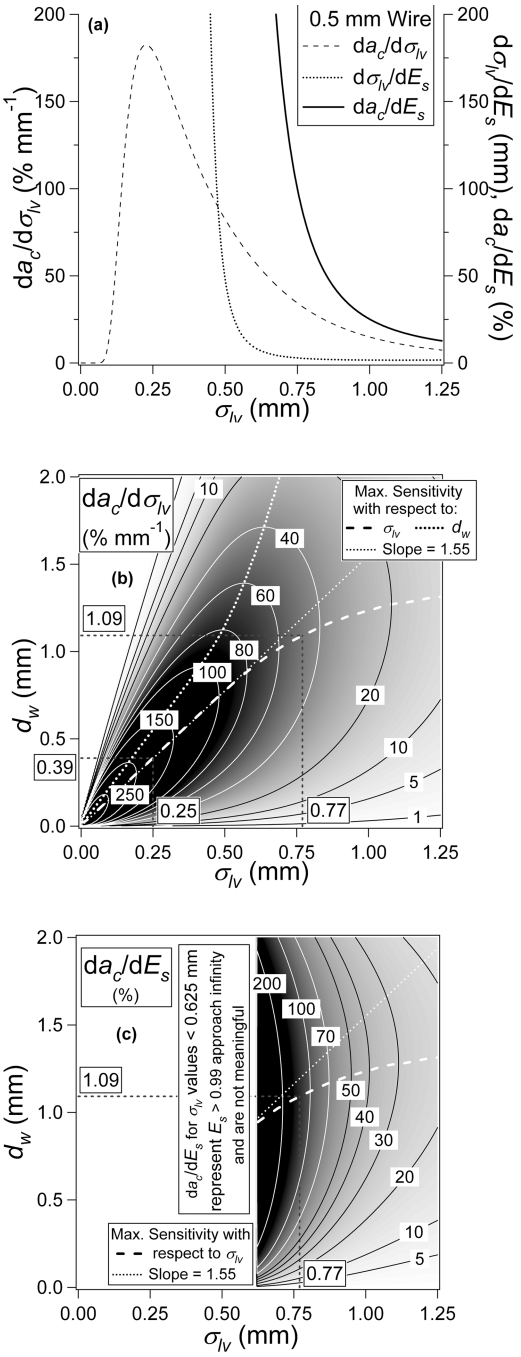

FIG. 10. Plots representing the sensitivity analysis for the wire-based beam width probe. (a) Summary for $d_w = 0.5$ mm, showing that da_c/dE_s can be found as the product of the other two curves. See text for explanation. (b) Image and contour plot of BWP sensitivity to σ_{lv} at the center wire position as a function of wire diameter and beam width. Maximum sensitivity with respect to σ_{lv} and to d_w for each wire diameter and beam size is shown (see text). The line of maximum sensitivity with respect to σ_{lv} fits a line of slope 1.55 (shown as straight line on the plot) until approximately $\sigma_{lv} = 0.6$ mm. (c) Image and contour plot of sensitivity to E_s. Note that for $\sigma_{lv} < 0.625$ mm the model produces unreasonable sensitivity values due to $d\sigma_{lv}/dE_s$ being very large, since E_s does not change in this regime (see Figure 4). The line of maximum sensitivity is the same as in (b).

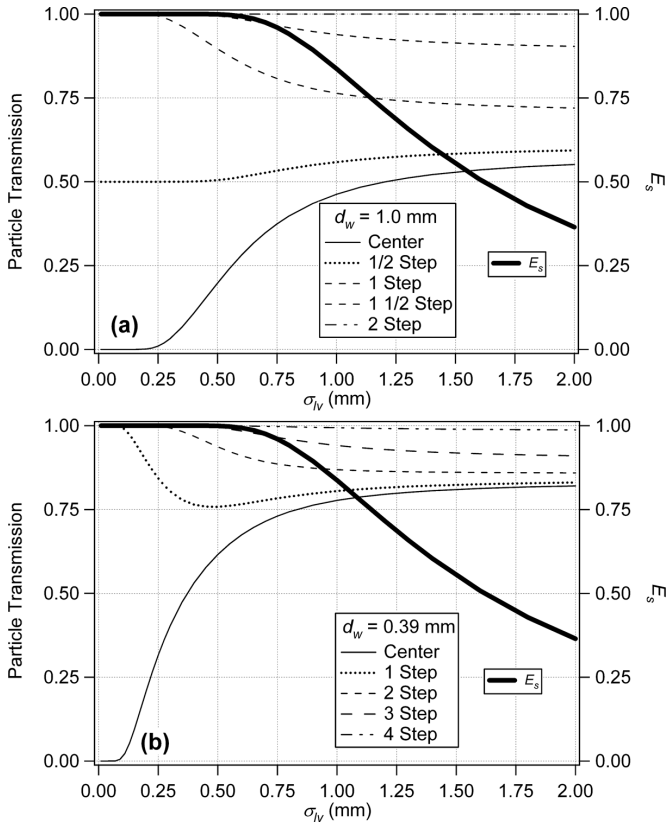

FIG. 11. Particle transmission and E_s vs. beam width σ_{lv} for different physical positions of the wire probe. Steeper regions of the curve have the most sensitivity, while flat regions show virtually no change in signal for a large difference in beam size. (a) Curves for $d_w = 1.0$ mm; optimal for wide beams, (b) curves for $d_w = 0.39$; optimal for narrow beams.

which is close to optimal for wide beams, and Figure 11b uses $d_w = 0.39$ mm, which is optimal for narrow beams. Curves in the figure represent the change in signal attenuation (as σ_{lv} changes) for a different physical location of the BWP, differing by full or $^1/_2$ diameters of the wire for each position (full-, half-step) of the probe. The bottom curve for each figure probes the center of the particle beam, where particle density, and resultant signal attenuation, is highest. Additional positions shown in the figure represent the attenuation at other probe locations. The areas of each curve with steeper slopes provide better sensitivity for beams of those σ_{lv}, because small changes in σ_{lv} produce significant changes in transmission. Areas that are nearly flat provide very little information about beam width because large changes in σ_{lv} cause only a small difference in transmission. For example a change in beam width between $\sigma_{lv} = 0.5$ and 0.75 mm in Figure 11a results in an easily detectable 18% change in absolute transmission at the center position, giving an average nominal sensitivity of 71%/mm. A change in beam width between 1.6 and 2.0 mm, however, only produces a harder to detect 1.7% change in absolute transmission, with a nominal sensitivity of 4.4%/mm. Figure 11a shows that a BWP of dimension 1.0 mm provides optimal information towards E_s, because the region of sensitivity for this probe is where E_s is less than one. A BWP of dimension 0.39 mm provides optimal information on particle shape for narrow beams, but has very little sensitivity for points with $E_s < 1$. This figure also illustrates the fact that the highest sensitivity is generally at the center position.

3.7. Results for AMS Short Chamber

As mentioned, these results are given for the long-chamber AMS, but can be extended to any other AMS chamber design, because for the same lens and particle type, the solid angle of the particle beam will be the same. Thus, the beam width at the vaporizer will be smaller in the short chamber by the ratio of the particle flight distances (Equation 3), i.e., $\sigma_{sv} = 0.77 \cdot \sigma_{lv}$. The width of the projection of the wire probe on the vaporizer surface will be $450/353 \cdot d_w$ for the long chamber, and $348/251 \cdot d_w$ for the short chamber. For the wire probe to block the same linear angle of particles, the width of the wire must be reduced according to the ratio the ratio of distances from lens to BWP. Thus, $d_{ws} = 0.71 \cdot d_{wl}$. Since the optimum wire for the long chamber was $d_{wl,opt} = 1.55 \cdot \sigma_{lv}$, the optimum wire for the short chamber can then be estimated as $d_{ws,opt} = 1.43 \cdot \sigma_{sv=} 1.10 \cdot \sigma_{lv}$, which corresponds to 0.28 and 0.85 mm for the canonical narrow (spheres) and wide (soot) beams, respectively. A wire diameter of 0.44 mm represents a compromise for the expected range of beam widths in ambient studies.

3.8. Alternative Probe Geometries

In addition to a moveable wire probe, we also considered three other probe geometries shown in Figure 12. The "transmission slit" consists of a surface that completely blocks the particle beam, with a vertical transmission slit cut down the center. The 'knife-edge' model uses a flat plate moved sequentially through the beam to block all points to the left of the edge. It effectively acts as the limit of a wire probe thicker than the vaporizer ($d_w > d_v$). The 'circular aperture' is a controllable circular opening centered on the vaporizer, with a larger vaporizer surface area blocked as the probe is close inwardly. Commercial laser alignment components may be available to implement this latter design.

The transmission slit is directly related to the wire probe. When the slit width and wire width are matched, the slit probe produces attenuation curves exactly the inverse of the wire probe model of the same width. Thus, there is not a major advantage of the slit compared to the wire probe, and the wire is preferred due to simpler construction and alignment. The knife-edge probe acts as an infinitely thick wire, and as discussed above it provides sub-optimal information as compared to wire probes with smaller d_w (see Figures 9–11), so it will not be discussed further. Using a second wire or knife-edge probe rotated 90 degrees would provide additional information about the particle beam in the other direction, which is of interest in practice since particle beams may not be perfectly circular. This alternative is not modeled here, because we are assuming a circular beam.

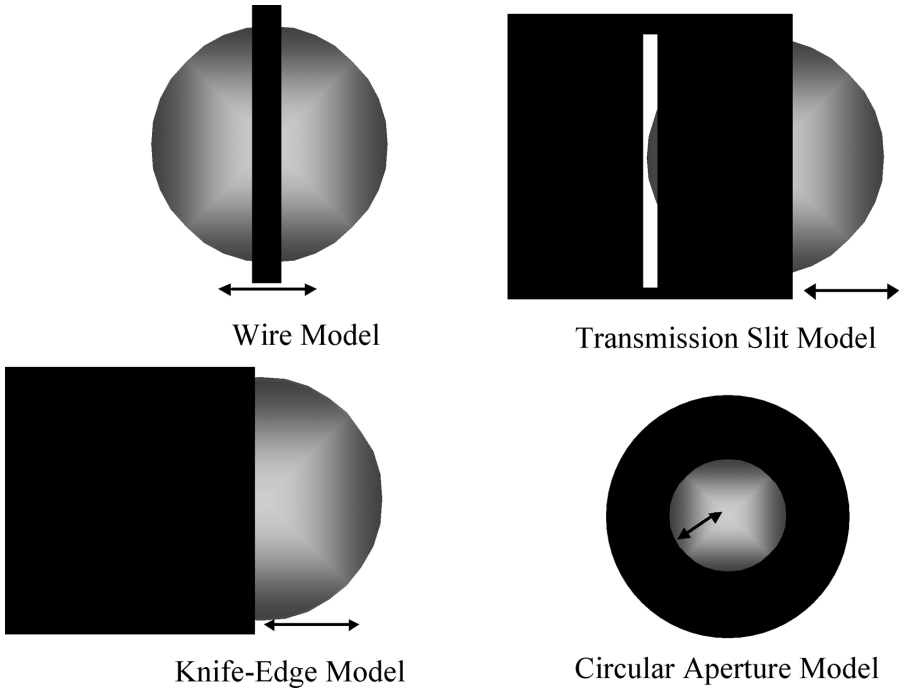

FIG. 12. Schematics of four alternative beam-width probe geometries (black) superimposed on the vaporizer (gray), including the wire probe geometry discussed so far, and the geometry of movement modeled for each.

Figure 13a shows the attenuation of the beam as a function of aperture radius for the variable aperture circular probe model, using the same σ_{lv} values as used in a similar curve for Figure 5a. Just as with the wire probe, the sensitivity with respect to beam width ($S'_\sigma = \mathrm{d}a_c/\mathrm{d}\sigma_{lv}$) can be numerically estimated by calculating the difference in signal transmission for two particle beams and dividing by the difference in σ_{lv}. Figure 13b plots the difference in curves for $\sigma_{lv} = 0.50$ & 0.52, and 1.00 & 1.02, as examples. $\mathrm{d}a_c/\mathrm{d}\sigma_{lv}$ is plotted in Figure 13c for the circular aperture (top line), as well as for two individual wire probes, and a line that represents the sensitivity of the optimal wire for each σ_{lv}. Note that this would mean changing the wire for optimal results in different σ_{lv} regions, and would therefore be impractical, but is shown for reference. The gain in sensitivity is shown on the right axis of Figure 13c. The circular aperture shows an increase in sensitivity by approximately 50–75% over the optimal wire at any given beam width, and considerably more for any one chosen wire. Thus, it would be desirable to use this probe instead of the wire-based probe. The circular aperture probe, however, may be difficult to implement in a high vacuum environment, and would be considerably more costly. Beam alignment would also become even more critical to the operation of the probe, and the complexities associated with different focusing beam center positions for different particle sizes (as described above) would be difficult to deconvolve from the data. On the other hand, the wire probe is by design "self-aligning." For these reasons, we currently advise the use of a wire-based probe with a wire diameter of 0.62 mm in the long AMS chamber (0.44 mm in the short chamber) in order to provide optimum sensitivity for measurement of σ_{lv} (and ψ and E_s) for ambient particles.

3.9. Estimation of Relative E_s for Other Particle Beam Instrument Geometries

The larger beam widths for non-spherical particles as compared to spherical ones can result in a potential detection bias for any instrument that uses aerodynamic lens inlets, with the spherical particles being detected more efficiently, and thus leading to a relative undercounting of the non-spherical ones. With the measurements performed with the AMS for various particle types and the model presented in this paper, we are in a position to estimate the relative bias for this instrument as well as for other instrument designs. Note that these are estimates based solely on the geometry of the particle flight length, and detector (or laser) size. We also assume that the slightly different Liu-type aerodynamic lenses used in instruments other than the AMS have similar beam broadening for non-spherical particles. We performed a theoretical estimation of the relative bias between spherical and other particle types for four common particle MS instruments. Beams comprised of perfectly spherical particles are detected with the highest efficiency by all instruments, because of the narrower distribution of particle radial locations. Figure 14a shows the shape-related collection efficiency (E_s) for the four instruments as a function of particle beam solid angle. Vertical lines are shown for oleic acid, ammonium nitrate, ammonium sulfate (Figure 8, this work), and

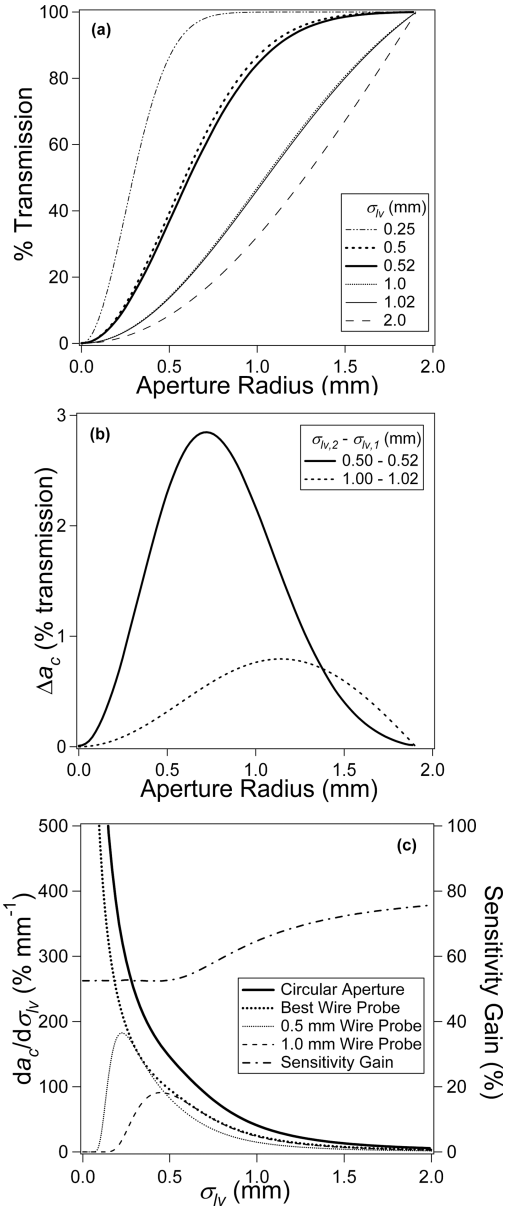

FIG. 13. (a) Transmission curve summary for the mathematical model of the circular aperture beam width probe. The radius of the aperture opening is the operational variable that can be changed, conceptually similar to the position of the wire probe. As the opening increases in size, the percentage of particle transmission increases as a function of the width of the particle beam (displayed on different lines). (b) The difference in attenuation signal (Δa_c) when the beam width changes is shown for two pairs of beam sizes as a function of aperture opening position. This mathematical difference is an intermediate step in determining the sensitivity ($da_c/d\sigma_{lv}$), values in the third panel. (c) $da_c/d\sigma_{lv}$ as a function of σ_{lv} is shown for the circular aperture probe, as well as for several wire probes, and for a line representing the optimal wire probe used at each σ_{lv} value. The sensitivity gain between the optimal wire probe, and the circular aperture is shown on the right axis.

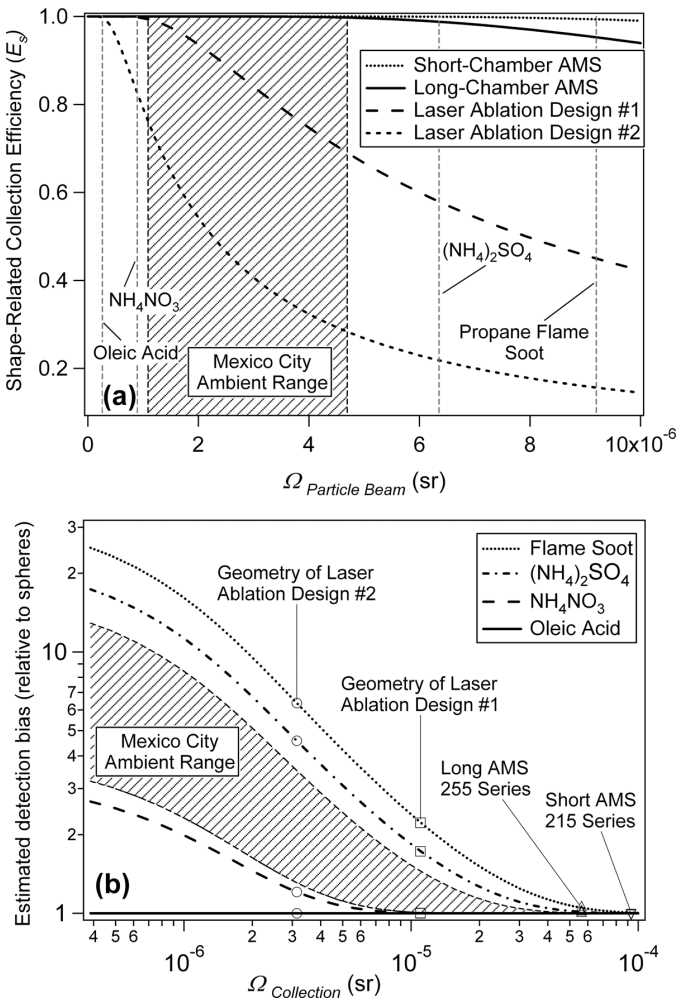

FIG. 14. Estimated relative detection bias between spherical particles and other particles types. (a) Shape-related collection efficiency (measured particle concentration divided by actual concentration) as a function of solid angle of particle beam. Each of four instruments defines a curve. Four laboratory-generated particle types are shown as vertical lines, and dashed region shows range of particle beam sizes observed in MCMA-2003 field campaign in Mexico City (Salcedo et al. 2005). (b) Estimated relative detection bias ($E_{s,spheres}/E_{s,irreg}$) between spherical particles and other particle types as a function of solid angle of collection. Each curve shows the relationship for a single particle type, with the dashed region showing the measured range from Mexico City. The points show the estimated biases for four particle MS instruments. Note that these are only predicted values based on the instrument geometry, and the model presented here, and have not been verified experimentally.

propane flame soot (Slowik et al. 2004), as well as for a range of ambient particles as seen in Mexico City (Salcedo et al. 2005). Figure 14b shows the relative instrument detection bias (with respect to spheres) as a function of solid angle of collection for the particle types shown in Figure 14a. As the solid angle of collection decreases (either because of smaller detector geometry, or longer flight path) the relative collection bias increases. For example the estimated detection bias to flame soot for the short-chamber AMS is approximately 1.007 (for $\Omega_{collection} = 9.31 \times 10^{-5}$), while the bias for the long-chamber AMS is 1.05 (for $\Omega_{collection} = 5.63 \times 10^{-5}$). The estimated detection bias to flame soot (and solid angle of collection) for laser ablation designs #1 and #2, are 2.22 (for $\Omega_{collection} = 1.10 \times 10^{-5}$) and 6.38 (for $\Omega_{collection} = 3.14 \times 10^{-6}$), respectively. Zelenyuk and

Imre (2005) have recently reported observing this shape bias with their laser-ablation mass spectrometer.

This increase in estimated detection bias arises from the fact that laser spot sizes are small, leading to relatively smaller solid angle of detection. The percentage of particles collected from a wide beam, therefore, is also small, and detection is sensitive to the particle beam width. The AMS has an advantage in this regard, because of its relatively large solid angle of collection, due to its large vaporization surface ($d_v = 3.81$ mm) as compared to typical laser spot sizes.

4. CONCLUSIONS

The use of aerodynamic lens inlets in aerosol mass spectrometers allows for efficient focusing of particles within a given size range, and has revolutionized the ability to analyze ambient particles in real time. Particles exit the lens as a tightly focused beam, but with finite divergence due to imperfect aerodynamic focusing, as well as Brownian motion and lift forces. The latter solely affect non-spherical particles, and so the focusing characteristics of a given particle type can be characterized by a surrogate non-sphericity parameter, ψ, the *lift shape factor*.

Ideally, all particles exiting the aerodynamic lens used in the AMS will impact onto the vaporizer surface in order to be evaporated and detected. It is important to have a quantitative measurement of the shape-related collection efficiency (E_s) in order to correct the measured mass concentrations for this effect. E_s is defined as the fraction of particles physically hitting the vaporizer, relative to spheres of the same vacuum aerodynamic diameter (d_{va}). This paper presents an analysis of a beam width probe designed to quantify ψ and E_s. The model is based on the assumption that the particle density is a circular two-dimensional Gaussian distribution. This assumption was validated experimentally for monodisperse single-component particles. The percentage of particles that miss detection due to a particle trajectory that misses the vaporizer (as compared to spheres of the same size) can then be calculated as a function of particle beam width. Spherical particles have $E_s = 1$ for both the long and short chamber AMS designs, whereas sufficiently irregular particles can be collected with less than unit efficiency, although these losses are small for current AMS designs even for the least focused particles that have been measured with the AMS (fractal soot, $E_s = 0.95$). This is an important conclusion from this work, because prior to the use of this model, it was estimated that collection losses arising from particle shape were significant.

Improvements in E_s for the AMS as a function of reductions in chamber length were estimated with the model. By reducing the distance from the lens exit to the particle vaporizer by 102 mm (450 mm to 348 mm) the E_s of fractal soot particles will increase from approximately 95% to more than 99%.

The model was then used to characterize the signal attenuation as a function of particle beam width for the beam width probe described here, and to optimize the beam width probe for the determination of σ_v (ψ) and E_s. The model shows that the optimum wire diameter for very irregular fractal soot particles with the AMS long chamber ($\sigma_{lv} \sim 0.77$ mm) is $d_w \sim 1.09$ mm, while the optimum wire probe diameter for beam width measurement of well-focused beams for nearly spherical particles ($\sigma_{lv} \sim 0.25$ mm) is $d_w \sim 0.39$ mm. An intermediate width of 0.6 mm (0.44 mm in the short chamber) is recommended for general-purpose measurements.

Three other probe geometries were also modeled and compared to the existing wire probe design. A knife-edge design provides sub-optimal sensitivity, while a transmission slit provides an exact inverse of the wire attenuation, but it is more cumbersome to implement. The circular aperture has sensitivity 50–75% greater than for any wire probe, but would also be more difficult to implement and operate reproducibly.

An estimate of particle detection efficiency of several mass spectrometer designs for several pure particle types, as well as for a range of ambient particles was calculated with respect to the collection of spherical particles. This estimated bias shows that as solid angle of collection decreases, the relative bias increases significantly, and that existing particle MS instruments show widely different behavior in terms of expected collection efficiency.

REFERENCES

Alfarra, M. R., Coe, H., Allan, J. D., Bower, K. N., Boudries, H., Canagaratna, M., Jimenez, J., Jayne, J., Garforth, A., Li, S. M., and Worsnop, D. (2004). Characterization of Urban and Rural Organic Particulate In the Lower Fraser Valley Using Two Aerodyne Aerosol Mass Spectrometers, *Atmos. Environ.* 38:5745–5758.

Allan, J. D., Bower, K. N., Coe, H., Boudries, H., Jayne, J. T., Canagaratna, M. R., Millet, D. B., Goldstein, A. H., Quinn, P. K., Weber, R. J., and Worsnop, D. R. (2004a). Submicron Aerosol Composition at Trinidad Head, California, during ITCT 2K2: Its Relationship With Gas Phase Volatile Organic Carbon and Assessment of Instrument Performance, *J. Geophys. Res. Atmos.* 109:(D23524), doi: 10.1029/2003JD004208.

Allan, J. D., Delia, A. E., Coe, H., Bower, K. N., Alfarra, M. R., Jimenez, J. L., Middlebrook, A. M., Drewnick, F., Onasch, T. B., Canagaratna, M. R., Jayne, J. T., and Worsnop, D. R. (2004b). A Generalised Method for the Extraction of Chemically Resolved Mass Spectra from Aerodyne Aerosol Mass Spectrometer Data, *J. Aerosol Sci.* 35(7):909–922.

Cziczo, P. J., DeMott, D. J., Brock, C., Hudson, P. K., Jesse, B., Kreidenweis, S. M., Prenni, A. J., Schreiner, J., Thomson, D. S., and Murphy, D. M. (2003). A Method for Single Particle Mass Spectrometry of Ice Nuclei, *Aerosol Sci. Technol.* 37(5):460–470.

DeCarlo, P., Slowik, J. G., Worsnop, D., Davidovits, P., and Jimenez, J. (2004). Particle Morphology and Density Characterization by Combined Mobility and Aerodynamic Diameter Measurements. Part 1: Theory, *Aerosol Sci. Technol.*, 38(12):1185–1205.

Delia, A. E., Real-Time Measurement of Non-Refractory Particle Composition and Interactions at Forested Sites, PhD Thesis, University of Colorado, Boulder, CO, 2004.

Drewnick, F., Hings, S. S., DeCarlo, P., Jayne, J., Gonin, M., Fuhrer, K., Weimer, S., Jimenez, J., Demerjian, K. L., Borrmann, S., and Worsnop, D. (2004). Application of a Novel Time-of-Flight Aerosol Mass Spectrometer for Chemical Composition Characterization of Urban (New York) aerosol, *Aerosol Sci. Technol.* 39(7):637–658.

Drewnick, F., Schwab, J. J., Hogrefe, O., Peters, S., Husain, L., Diamond, D., Weber, R., and Demerjian, K. L.(2003). Intercomparison and Evaluation of Four Semi-Continuous PM2.5 Sulfate Instruments, *Atmos. Environ.* 37(24):3335–3350.

Gard, E., Mayer, J. E., Morrical, B. D., Dienes, T., Fergenson, D. P., and Prather, K. A. (1997). Real-Time Analysis of Individual Atmospheric Aerosol Particles: Design and Performance of a Portable ATOFMS, *Anal. Chem.* 69(20):4083–4091.

Heberlein, J., Postel, O., Girshick, S., McMurry, P., Gerberich, W., Iordanoglou, D., Di Fonzo, F., Neumann, D., Gidwani, A., Fan, M. and Tymiak, N. (2001). Thermal Plasma Deposition of Nanophase Hard Coatings, *Surface & Coatings Technology*, 142:265–271.

Hogrefe, O., Schwab, J. J., Drewnick, F., Lala, G. G., Peters, S., Demerjian, K. L., Rhoads, K. P., Felton, H. D., Rattigan, O. V., Husain, L., and Dutkiewicz, V. A. (2004). Semicontinuous PM2.5 Sulfate and Nitrate Measurements at an Urban and a Rural Location in New York: PMTACS-NY Summer 2001 and 2002 Campaigns, *J. Air & Waste Manage. Assoc.* 54:1040–1060.

Jayne, J. T., Leard, D. C., Zhang, X. F., Davidovits, P., Smith, K. A., Kolb, C. E., and Worsnop, D. R. (2000). Development of an Aerosol Mass Spectrometer for Size and Composition Analysis of Submicron Particles, *Aerosol Sci. Technol.* 33(1–2):49–70.

Jimenez, J., Seinfeld, J. H., Flagan, R. C., Canagaratna, M., Jayne, J., Worsnop, D., Zhang, X., and Smith, K. A. (2001). Size Resolution of the Aerodyne Aerosol Mass Spectrometer, in *AAAR Annual Meeting*, Portland, Oregon, 2001.

Jimenez, J. L., Bahreini, R., Cocker, D. R., Zhuang, H., Varutbangkul, V., Flagan, R. C., Seinfeld, J. H., O'Dowd, C. D., and Hoffmann, T. (2003a). New particle Formation from Photooxidation of Diiodomethane (CH2I2), *J. Geophys. Res. Atmos.* 108:(D10): 4318, doi: 10.1029/2001JD001213.

Jimenez, J. L., Jayne, J. T., Shi, Q., Kolb, C. E., Worsnop, D. R., Yourshaw, I., Seinfeld, J. H., Flagan, R. C., Zhang, X. F., Smith, K. A., Morris, J. W., and Davidovits, P. (2003b). Ambient Aerosol Sampling Using the Aerodyne Aerosol Mass Spectrometer, *J. Geophys. Res. Atmos.* 108:(D10): 4318, doi: 10.1029/2002JD002452.

Kane, D. B., and Johnston, M. V. (2000). Size and Composition Biases on the Detection of Individual Ultrafine Particles by Aerosol Mass Spectrometry, *Environ. Sci. Technol.* 34(23):4887–4893.

Katrib, Y., Martin, S., Rudich, Y., Davidovits, P., Jayne, J., and Worsnop, D. (2005). Density Changes of Aerosol Particles as a Result of Chemical Reactions, *Atmos. Chem. Phys.* 5:275–291.

Liu, P., Ziemann, P. J., Kittelson, D. B., and McMurry, P. H. (1995a). Generating Particle Beams of Controlled Dimensions and Divergence .1. Theory of Particle Motion in Aerodynamic Lenses and Nozzle Expansions, *Aerosol Sci. Technol.* 22(3):293–313.

Liu, P., Ziemann, P. J., Kittelson, D. B., and McMurry, P. H. (1995b). Generating Particle Beams of Controlled Dimensions and Divergence .2. Experimental Evaluation of Particle Motion in Aerodynamic Lenses and Nozzle Expansions, *Aerosol Sci. Technol.* 22(3):314–324.

Mahadevan, R., Lee, D., Sakurai, H., and Zachariah, M. R. (2002). Measurement of Condensed-Phase Reaction Kinetics in the Aerosol Phase Using Single Particle Mass Spectrometry, *J. Phys. Chem. A* 106(46):11083–11092.

Middlebrook, A. M., and Matthew, B. (2004). Personal Communication.

Oktem, B., Tolocka, M. P., and Johnston, M. V. (2004). On-Line Analysis of Organic Components in Fine and Ultrafine Particles by Photoionization Aerosol Mass Spectrometry, *Anal. Chem.* 76(2):253–261.

Onasch, T.B. (2004). Personal Communication.

Petrucci, G. A., Farnsworth, P. B., Cavalli, P., and Omenetto, N. (2000). A Differentially Pumped Particle Inlet for Sampling of Atmospheric Aerosols into a Time-of-Flight Mass Spectrometer: Optical Characterization of the Particle Beam, *Aerosol Sci. Technol.* 33(1–2):105–121.

Salcedo, D., Dzepina, K., Huffman, J. A., DeCarlo, P., Jimenez, J. L., Onasch, T. B., Jayne, J. T., Mortimer, P., and Worsnop, D. (2005). Characterization of Ambient Aerosols in Mexico City using an Aerosol Mass Spectrometer, *Atmos. Chem. Phys.* 5:4143–4182.

Schreiner, J., Schild, U., Voigt, C., and Mauersberger, K. (1999). Focusing of Aerosols into a Particle Beam at Pressures from 10 to 150 Torr, *Aerosol Sci. Technol.* 31(5):373–382.

Schreiner, J., Voigt, C., Mauersberger, K., McMurry, P., and Ziemann, P. (1998). Aerodynamic Lens System for Producing Particle Beams at Stratospheric Pressures, *Aerosol Sci. Technol.* 29(1):50–56.

Schreiner, J., Voigt, C., Zink, P., Kohlmann, A., Knopf, D., Weisser, P., Budz, C.,and Mauersberger, K. (2002). A Mass Spectrometer System for Analysis of Polar Stratospheric Aerosols, *Review of Scientific Instruments* 73(2):446–452.

Serway, R. A. (1996). *Physics For Scientists and Engineers*, Saunders College Publishing, pp. 696.

Slowik, J. G., Stainken, K., Davidovits, P., Williams, L. R., Jayne, J., Kolb, C. E., Worsnop, D., Rudich, Y., DeCarlo, P., and Jimenez, J. (2004). Particle Morphology and Density Characterization by Combined Mobility and Aerodynamic Diameter Measurements. Part 2: Application to Combustion Generated Soot Particles as a Function of Fuel Equivalence Ratio, *Aerosol Sci. Technol.* 28(12):1206–1222.

Su, Y. X., Sipin, M. F., Furutani, H., and Prather, K. A. (2004). Development and Characterization of an Aerosol Time-of-Flight Mass Spectrometer with Increased Detection Efficiency, *Anal. Chem.* 76(3):712–719.

Svane, M., Hagstrom, M., and Pettersson, J. B. C. (2004). Chemical Analysis of Individual Alkali-Containing Aerosol Particles: Design and Performance of a Surface Ionization Particle Beam Mass Spectrometer, *Aerosol Sci. Technol.* 38(7):655–663.

Sykes, D. C., Woods, E., Smith, G. D., Baer, T., and Miller, R. E. (2002). Thermal Vaporization-Vacuum Ultraviolet Laser Ionization Time-of-Flight Mass Spectrometry of Single Aerosol Particles, *Anal. Chem.* 74(9):2048–2052.

Tafreshi, H. V., Benedek, G., Piseri, P., Vinati, S., Barborini, E., and Milani, P. (2002). A Simple Nozzle Configuration for the Production of Low Divergence Supersonic Cluster Beam by Aerodynamic Focusing, *Aerosol Sci. Technol.* 36(5):593–606.

Tobias, H. J., Kooiman, P. M., Docherty, K. S., and Ziemann, P. J. (2000). Real-Time Chemical Analysis of Organic Aerosols Using a Thermal Desorption Particle Beam Mass Spectrometer, *Aerosol Sci. Technol.* 33(1–2):170–190.

Weimer, S., Drewnick, F., Hogrefe, O., Schwab, J. J., Rhoads, K. P., Orsini, D. A., Canagaratna, M., Worsnop, D., and Demerjian, K. L. (2005). Size-Selective Non-Refractory Ambient Aerosol Measurements During the PMTACS-NY 2004 Winter Intensive in New York City. In Preparation.

Zelenyuk, A., and Imre, D. (2005). Single Particle Laser Ablation Time-of-Flight Mass Spectrometer: An Introduction of SPLAT, *Aerosol Sci. Technol.* 39(6):554–568.

Zelenyuk, A., Cabalo, J., Baer, T., and Miller, R. E. (1999). Mass Spectrometry of Liquid Aniline Aerosol Particles by IR/UV Laser Irradiation, *Anal. Chem.* 71(9):1802–1808.

Zhang, Q., Canagaratna, M., Jayne, J., Worsnop, D., and Jimenez, J. (2004a). Time and Size-Resolved Chemical Composition of Submicron Particles in Pittsburgh-Implications for Aerosol Sources and Processes, *J. Geophys. Res.—Atmos.* 110 (D7), D07S09, doi: 10.1029/2004JD004649.

Zhang, Q., Stanier, C. O., Canagaratna, M., Jayne, J., Worsnop, D., Pandis, S. N., and Jimenez, J. (2004b). Insights into the Chemistry of Nucleation Bursts and New Particle Growth Events in Pittsburgh Based on Aerosol Mass Spectrometry, *Environ. Sci. Technol.* 38:4797–4809.

Zhang, X. F., Smith, K. A., Worsnop, D. R., Jimenez, J., Jayne, J. T., and Kolb, C. E. (2002). A Numerical Characterization of Particle Beam Collimation by an Aerodynamic Lens-Nozzle System: Part I. An Individual Lens or Nozzle, *Aerosol Sci. Technol.* 36(5):617–631.

Zhang, X. F., Smith, K. A., Worsnop, D. R., Jimenez, J. L., Jayne, J. T., Kolb, C. E., Morris, J., and Davidovits, P. (2004c). Numerical Characterization of Particle Beam Collimation: Part II–Integrated Aerodynamic-Lens-Nozzle System, *Aerosol Sci. Technol.* 38(6):619–638.

Zhang, Y. (2004). *Indoor Air Quality*, CRC Press, Boca Raton, FL.

APPENDIX A

List of terms and symbols:

BWP beam width probe

σ	standard deviation of Gaussian distribution	d_v	diameter of vaporizer surface (3.81 mm)
σ_v	particle beam width (one standard deviation) at the vaporizer	d_w	wire probe diameter
σ_{lv}	particle beam width at the vaporizer for the long AMS chamber	Ω	solid angle
σ_{sv}	particle beam width at the vaporizer for the short AMS chamber	Ω_{beam}	solid angle a particle beam encompassed (at 1σ)
σ_{lw}	particle beam width at the BWP for the long AMS chamber	$\Omega_{collection}$	solid angle of collection for an instrument
σ_{sw}	particle beam width at the BWP for the short AMS chamber	ψ	lift shape factor
$\sigma_p^{d_{va}}$	particle beam width for a given particle, of a given size	χ	dynamic shape factor
$\sigma_{sph}^{d_{va}}$	particle beam width for spherical particles, of a given size	S	Jayne shape factor
σ_{1DG}	standard deviation of 1-dimensional Gaussian data fit	d_{va}	vacuum aerodynamic diameter
L	AMS chamber length (from nozzle exit to vaporizer)	d_{max}	largest particle size to be sampled
L_l	AMS chamber length for long AMS chamber (450 mm)	CE	overall instrumental collection efficiency
r_v	radius of vaporizer surface (1.905 mm)	E_b	collection efficiency due to the effect of particle bounce at the vaporizer surface
		E_s	collection efficiency due to the effect of particle shape in beam width
		E_L	transmission efficiency due to focusing effects in the aerodynamic lens
		a_c	particle beam attenuation at the center of the beam
		S_σ	sensitivity of the attenuation signal to a change in beam width
		S_{Es}	sensitivity to E_s